Structural and Mechanistic Changes along an Engineered Path from Metallo to Nonmetallo 3-Deoxy-D-*manno*-octulosonate 8-Phosphate Synthases[†,‡]

Fathima Kona,[§] Xingjue Xu,[§] Philip Martin, Petr Kuzmic,[||] and Domenico L. Gatti*

Department of Biochemistry and Molecular Biology, Wayne State University School of Medicine, Detroit, Michigan 48201

Received December 3, 2006; Revised Manuscript Received February 21, 2007

ABSTRACT: There are two classes of KDO8P synthases characterized respectively by the presence or absence of a metal in the active site. The nonmetallo KDO8PS from *Escherichia coli* and the metallo KDO8PS from *Aquifex aeolicus* are the best characterized members of each class. All amino acid residues that make important contacts with the substrates are conserved in both enzymes with the exception of Pro-10, Cys-11, Ser-235, and Gln-237 of the *A. aeolicus* enzyme, which correspond respectively to Met-25, Asn-26, Pro-252, and Ala-254 in the *E. coli* enzyme. Interconversion between the two forms of KDO8P synthases can be achieved by substituting the metal-coordinating cysteine of metallo synthases with the corresponding asparagine of nonmetallo synthases, and vice versa. In this report we describe the structural changes elicited by the C11N mutation and by three combinations of mutations (P10M/C11N, C11N/S235P/Q237A, and P10M/C11N/S235P/Q237A) situated along possible evolutionary paths connecting the *A. aeolicus* and the *E. coli* enzyme. All four mutants are not capable of binding metal and lack the structural asymmetry among subunits with regard to substrate binding and conformation of the L7 loop, which is typical of *A. aeolicus* wild-type KDO8PS but is absent in the *E. coli* enzyme. Despite the lack of the active site metal, the mutant enzymes display levels of activity ranging from 46% to 24% of the wild type. With the sole exception of the quadruple mutant, metal loss does not affect the thermal stability of KDO8PS. The free energy of unfolding in water is also either unchanged or even increased in the mutant enzymes, suggesting that the primary role of the active site metal in *A. aeolicus* KDO8PS is not to increase the enzyme stability. In all four mutants A5P binding displaces a water molecule located on the *si* side of PEP. In particular, in the double and triple mutant, A5P binds with the aldehyde carbonyl in hydrogen bond distance of Asn-11, while in the wild type this functional group points away from Cys-11. This alternative conformation of A5P is likely to have functional significance as it resembles the conformation of the acyclic reaction intermediate, which is observed here for the first time in some of the active sites of the triple mutant. The direct visualization of this intermediate by X-ray crystallography confirms earlier mechanistic models of KDO8P synthesis. In particular, the configuration of the C2 chiral center of the intermediate supports a model of the reaction in nonmetallo KDO8PS, in which water attacks an oxocarbenium ion or PEP from the *si* side of C2. Several explanations are offered to reconcile this observation with the fact that no water molecule is observed at this position in the mutant enzymes in the presence of both PEP and A5P. Significant differences were observed between the wild-type and the mutant enzymes in the K_m values for PEP and A5P and in the K_d values for inorganic phosphate and R5P. These differences may reflect an evolutionary adaptation of metallo and nonmetallo KDO8PS's to the cellular concentrations of these metabolites in their respective hosts.

KDO8P synthase (KDO8PS,[1] EC 4.1.2.16) is a key enzyme for lipopolysaccharide biosynthesis in Gram-negative bacteria (*1*, *2*). It catalyzes the aldol-like condensation of phosphoenolpyruvate (PEP) and arabinose 5-phosphate (A5P) to form the 8-carbon sugar 3-deoxy-D-*manno*-octulosonate 8-phosphate (KDO8P) (*3*). The reaction requires one molecule of water and proceeds through the formation of a doubly phosphorylated acyclic intermediate that decays into KDO8P and inorganic phosphate (P_i) (*4*−*6*) (Figure 1). The intermediate is formed upon attack of the *si* face of $C3^{PEP}$ on the *re* face of $C1^{A5P}$; phosphate release occurs by cleavage of the C−O rather than the P−O bond, such that the anomeric oxygen of KDO8P derives from solvent (*7*−*9*). It

[†] This research was supported by U.S. Public Health Service Grant GM69840 to D.L.G.

[‡] The structure factor amplitudes and the refined coordinates of C11N + PEP, PEP + A5P, PEP + R5P, P10M/C11N + PEP, C11N/S235P/Q237A + PEP, PEP + A5P (form C and form D), and P10M/C11N/S235P/Q237A + PEP + A5P were deposited in the Protein Data Bank (entries 2NWR, 2NWS, 2NX1, 2NXI, 2NXH, 2NX3, 2NXG, and 2EF9, respectively).

* Corresponding author. Tel: (313) 577-0620. Fax: (313) 577-2765. E-mail: mimo@boatman.med.wayne.edu.

[§] These authors have contributed equally to the work.

[||] Present address: BioKin, Ltd., P.O. Box 666, Pullman, WA 99163.

[1] Abbreviations: GdnHCl, guanidine hydrochloride; KDO, 3-deoxy-D-*manno*-octulosonate; KDO8P, 3-deoxy-D-*manno*-octulosonate 8-phosphate; KDO8PS 3-deoxy-D-*manno*-octulosonate 8-phosphate synthase; PEP, phosphoenolpyruvate; A5P, arabinose 5-phosphate; R5P, ribose 5-phosphate; EDTA, ethylenediaminetetraacetic acid; INT, tetrahedral reaction intermediate; OXO, oxocarbenium ion; RMSD, root mean square deviation; NCS, noncrystallographic symmetry; H, helix; S, strand; L, loop.

10.1021/bi6024879 CCC: $37.00
Published on Web 03/24/2007

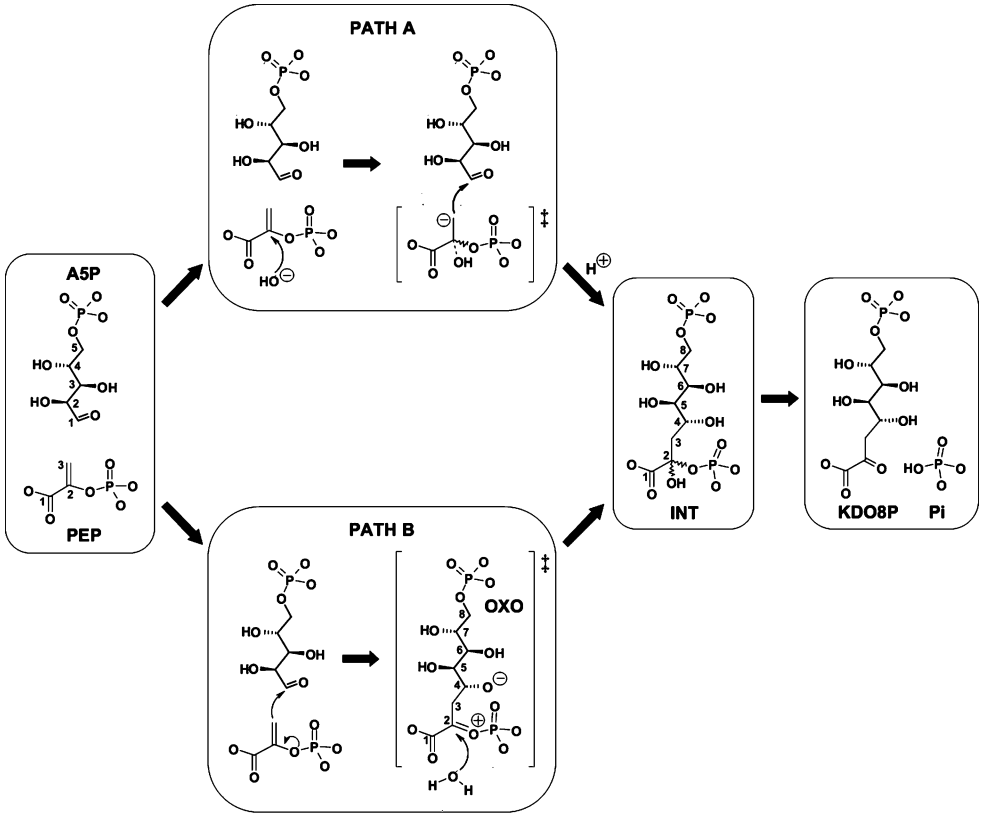

FIGURE 1: Biosynthesis of 3-deoxy-D-*manno*-octulosonic acid (KDO8P) from arabinose 5-phosphate (A5P) and phosphoenolpyruvate (PEP). Path A: Attack by a hydroxide ion on $C2^{PEP}$ leads to a transient carbanion at $C3^{PEP}$ that reacts with $C1^{A5P}$. Transient species are in brackets and are marked with a double dagger (‡) symbol. Charges on the carboxylate and phosphate moieties are not shown. Path B: The postulated acyclic tetrahedral reaction intermediate (INT) is formed stepwise via a transient oxocarbenium ion (OXO) that reacts with water.

is not known whether the expected attack by water (or a hydroxide ion) onto $C2^{PEP}$ occurs prior to or after the formation of the bond between $C3^{PEP}$ and $C1^{A5P}$ (see paths A and B of Figure 1, respectively) (*6*, *10*). The phylogenetic tree of KDO8PS is evenly divided between two forms of the enzyme characterized by the absence or presence of a metal ion in the active site (*11*, *12*). We and others have determined the crystal structure of one nonmetallo form (from *Escherichia coli*) and of one metallo form (from *Aquifex aeolicus*) (*5*, *13*−*15*). While there is no structure of a nonmetallo KDO8PS in complex with both PEP and A5P, we have reported several structures of both wild-type and mutant KDO8PS from *A. aeolicus* complexed with both substrates (*5*, *16*, *17*). On the basis of these structures, we have proposed that in metallo KDO8PS a metal-bound water located on the *si* side of PEP dissociates to a hydroxide ion that attacks $C2^{PEP}$; the ensuing carbanion at $C3^{PEP}$ would then facilitate attack onto $C1^{A5P}$ (path A of Figure 1). Kaustov et al. and Asojo et al. (*18*, *19*), largely on the basis of studies of the nonmetallo *E. coli* enzyme, favor a different stepwise mechanism in which bond formation between $C3^{PEP}$ and $C1^{A5P}$ leads to the formation of an oxocarbenium intermediate followed by reaction with water from either the *si* or the *re* side of C2 and phosphate release (path B in Figure 1). Additional arguments against path A are based on studies in which the single cysteine ligand of the active site metal of a metallo KDO8PS has been replaced with asparagine, the residue universally conserved at the same position in nonmetallo KDO8P synthases (*20*−*22*). Naturally occurring nonmetallo KDO8P synthases are as active as their metallo counterparts, and nonmetallo synthases engineered via Cys → Asn substitution still maintain considerable activity. Thus, it has been inferred that the metal ion is not necessary for catalysis or that at best it serves an auxiliary role in assuring the proper orientation of the reacting species. Although a direct structural investigation of a genetically engineered metal-free variant of KDO8P synthase has not been carried out, comparison between the structures of *A. aeolicus* and *E. coli* enzymes reveals that at least three other residues, in addition to the metal-coordinating cysteine, may be involved in defining the transition between metallo and nonmetallo synthases. A superposition of *A. aeolicus* and *E. coli* KDO8PS shows that most of the residues that line the active site cavity are conserved in both enzymes with the notable exception of Pro-10, Cys-11, Ser-235, and Gln-237 of the *A. aeolicus* enzyme, which correspond respectively to Met-25, Asn-26, Pro-252, and Ala-254 in the *E. coli* enzyme (Table 1). Pro-10 and Cys-11 are located at the end of the S1 strand; Ser-235 and Gln-237 are near the end of the L8 loop. All four residues appear to influence the conformation of the L2, L7, and L8 loops. In *A. aeolicus* the carboxamide moiety of Gln-237 is hydrogen bonded to the backbone of Cys-11. The corresponding Ala-254 in *E. coli* leaves a cavity near Asn-26 (Cys-11 in *A. aeolicus*), which is filled by water. In *E. coli*, the L8 loop is slightly bent by Pro-252 (Ser-235 in *A. aeolicus*), which changes the orientation of Asp-250 (Asp233, a metal ligand, in *A. aeolicus*). Interestingly, all of the enzymes that contain respectively Asn, Pro, and Ala at the positions of Cys-11, Ser-235, and Gln-237 of the *A. aeolicus* enzyme are nonmetallo KDO8PS's. As already noted by Oliynyk et al. (*21*), in almost all metallo KDO8PS's there is a Pro immediately preceding the Cys that is a metal

Table 1: Equivalent Residues in *A. aeolicus* and *E. coli* KDO8PS Active Sites[a]

A. aeolicus	*E. coli*	*A. aeolicus*	*E. coli*
Pro-10	**Met-25**	Lys-124	Lys-138
Cys-11	**Asn-26**	Arg-154	Arg-168
Lys-46	Lys-60	Asp-182	Asp-199
Arg-49	Arg-63	His-185	His-202
Ser-51	Ser-64	Gln-188	Gln-205
Asp-81	Asp-95	Glu-222	Glu-239
His-83	His-97	Asp-233	Asp-250
Gln-99	Gln-113	**Ser-235**	**Pro-252**
Phe-103	Phe-117	**Gln-237**	**Ala-254**

[a] Different kinds of residues are shown in bold.

ligand. A methionine is universally present in nonmetallo synthases at this position, with the notable exception of KDO8PS's from higher plants (e.g., *Arabidopsis thaliana*). The cavity occupied by the bulky methionine side chain of the *E. coli* enzyme is filled in *A. aeolicus* by a combination of the proline ring *plus* the backbone kink introduced by this residue. The final effect is almost identical, with the sulfur atom of Cys-11 of the *A. aeolicus* enzyme occupying almost the same relative position in space as the β-carbon of Asn-26 in the *E. coli* enzyme. Thus, positions 11 (Cys-11) and 235 (Ser-235) of the *A. aeolicus* enzyme appear to be the two most important positions to achieve the formation of the metal center, with positions 237 (Gln-237) and 10 (Pro-10) being accessory in optimizing the orientation of Cys-11. In this study we describe four mutant enzymes, which may represent different steps along an evolutionary pathway connecting metallo and nonmetallo KDO8PS, namely, C11N, P10M/C11N, C11N/S235P/Q237A, and P10M/C11N/S235P/Q237A. These mutant proteins have in common the C11N substitution, and throughout this report we refer to them cumulatively as the "C11N series". All of the enzymes of the series were analyzed with respect to their stability, kinetic properties, and three-dimensional structure. While it was not possible to discriminate between path A and path B of KDO8P synthesis (Figure 1), an important conclusion of this study, based on the direct observation, for the first time, of the reaction intermediate, is that the reaction requires the participation of a water molecule located on the *si* side of PEP. This water molecule can tentatively be identified as one that in the wild type is coordinated to the active site metal and in the enzymes of the C11N series is hydrogen bonded to Asn-11.

EXPERIMENTAL PROCEDURES

Protein Production and Purification. A. aeolicus KDO8PS was produced in *E. coli* from plasmid pet28a/*kdsa*, which was derived from plasmid pet28a (Novagen) by inserting the *A. aeolicus* KDSA gene in frame with the ATG of the vector *Nco*I site. Plasmids pet28a/*kdsaC11N*, pet28a/*kdsaP10MC11N*, pet28a/*kdsaC11N S235PQ237A*, pet28a/*kdsaP10MC11N S235PQ237A* encoding the mutant proteins were derived from the wild-type encoding plasmid by replacing the Pro codon CCC with the Met codon, the Cys codon TGC with the Asn codon AAC, the Ser codon TCA with the Pro codon CCA, and the Gln codon CAG with the Ala codon GCG using the Quick-Change (Stratagene) mutagenesis system. Both the wild-type and mutant proteins were purified as described by Xu et al. (*17*). Cd^{2+}, Zn^{2+}, and metal-free wild-type KDO8PS were obtained by dialyzing for 24 h the purified enzyme against 20 mM Tris-HCl (pH 7.5) containing 50 μM Cd^{2+} or Zn^{2+} and 5 mM EDTA, respectively.

Stability Measurements. (A) Thermal Denaturation. Thermal stability of wild-type and mutant KDO8PS was determined by measuring the changes in the far-UV region (190−250 nm range, 1 nm intervals) of the circular dichroism spectrum of the enzyme during a 20−90 °C temperature ramp. The ramp was developed over a 1 h period at 5 °C intervals. Spectra were recorded with a 0.5 mm path quartz cuvette in water at the protein concentration of 0.2−0.34 mg/mL with an Olis DSM17 CD spectrometer equipped with a Peltier cell. Singular value decomposition (SVD) of the contributing spectral components corresponding to the folded and unfolded protein was carried out with the OLIS GlobalWorks software suite. Both two-state (native → unfolded) and three-state (native → intermediate → unfolded) models with constant or variable enthalpy over temperature were tested to identify the best fit of the experimental data.

(B) Chemical Denaturation. KDO8PS (1 μM) was incubated in 20 mM Tris-HCl, pH 8.0, and 150 mM NaCl (plus 50 μM Cd^{2+} or Zn^{2+} in the case of the wild-type enzyme) supplemented with increasing amounts of GdnHCl at 23 °C overnight. Equilibrium was reached during this time period. The concentration of GdnHCl in each experimental sample (0−6.5 M range) was determined from its refractive index (*23*). Intrinsic fluorescence emission spectra were recorded at 23 °C between 300 and 400 nm following excitation at 280 nm. Slit widths were set at 2.0 nm.

The red shift in intrinsic fluorescence emission spectra at increasing GdnHCl concentrations was quantified as the intensity-averaged emission wavelength, λ_{avg} (*24*). Baseline and transition-region data for the GdnHCl equilibrium denaturation curve were fitted with SigmaPlot to a two-state linear-extrapolation model (*25*) according to eq 1,where ΔG_u is the free energy change for unfolding at a given denaturant (GdnHCl) concentration, ΔG^{H_2O} is the free energy change for unfolding in the absence of denaturant, m is a slope term that equates the change in ΔG_u per unit concentration of GdnHCl, R is the gas constant (1.987 cal mol^{-1} K^{-1}), T is the temperature (296.15 K), and K_u is the equilibrium constant for unfolding.

$$\Delta G_u = \Delta G^{H_2O} - m[D] = -RT \ln K_u \qquad (1)$$

Enzymatic Activity. Rate constants for the reaction catalyzed by KDO8PS were determined by nonlinear regression analysis (*26*) of multiple progress curves of PEP consumption at 40 °C. The curves were recorded at 232 nm (ϵ^{PEP} = 2840 M^{-1} cm^{-1}) when the enzyme (1−2 μM) was added to a solution containing 100 mM Tris−acetate (pH 7.5) and several different concentrations and molar ratios of PEP, A5P (and/or R5P), and P_i, as described by Xu et al. (*17*). $CdCl_2$ (50 μM) was added to the reaction mixture containing the wild-type enzyme. The ensemble of curves was analyzed globally [simultaneous fit of all of the progress curves (*27*)] for each enzyme form using the program Dynafit (*28*). In the case of the reaction occurring in the presence of only PEP and A5P, the global least-squares fit was based on the stepwise refinement of all adjustable model parameters. Each progress curve consisted of 100 points, for a total of 1900

points (19 curves) in each data set. According to the theory of statistical estimation (*29*), this is a more than sufficient number of data points to determine uniquely all adjustable model parameters (rate constants, protein/PEP/A5P/P_i concentrations; see Tables 4 and 5, below).

In the case of reactions occurring in the presence of both A5P and R5P the rate constants for the steps involving A5P were fixed at the values identified in the above experiments, and only the rate constants related to steps involving R5P were refined.

Structure Determination and Refinement. Crystals of *A. aeolicus* KDO8PS were obtained as described previously (*5*, *30*). The crystals used in this study belong to two different space groups: $P3_121$ and $P2_1$ (Table 2). Oscillation data were collected at 100 K with an HTC image plate detector at the Cu Kα wavelength, or with a Quantum4 detector at the BIOCARS 14-ID beamline of the Advanced Photon Source, and processed with HKL (*31*). All structure determinations were carried out with CNS v.1.1 using cross-validated maximum likelihood as the target function (*32*). As crystals of sg $P3_121$ are highly isomorphous to those of the wild type, standard crystallographic refinement starting from the wild-type model was sufficient to determine the structure. For crystals of sg $P2_1$, a molecular replacement procedure was employed using the wild-type tetramer as the starting model. A single cross-rotation function and three consecutive translation function analyses were carried out to position three tetramers in the asymmetric unit. Rigid body and simulated annealing refinement were then sufficient to determine the overall structure of the mutant. All 12 chains were refined independently without NCS restraints. In all cases, after verifying the presence of the expected mutations and correcting the model accordingly, water molecules were added by means of several cycles of the automated routine for water identification available in CNS. Each cycle of automated water addition was followed by a visual examination of the model.

RESULTS

Stability of Wild-Type and Mutant KDO8P Synthases. On the basis of studies of the homologous metalloenzyme 3-deoxy-D-*arabino*-heptulosonate 7-phosphate (DAH7P synthase, DAH7PS), substituted with different metal ions, Furdui et al. (*10*) have suggested that in this class of enzymes the metal ion serves primarily a structural function, perhaps adding stability. In view of Furdui's suggestion, and because *A. aeolicus* KDO8PS is purified via a heat step at 80 °C (*17*), it was of interest to determine whether the thermal stability of the mutant enzymes, which all lack a metal in the active site (see below), differs from that of the wild type. For this purpose we recorded the CD spectral changes in the far-UV region incurred by KDO8PS during a temperature ramp from 20 to 90 °C. No conformational transition was observed in the wild type and in the three mutants C11N, P10M/C11N, and C11N/S235P/Q237A, which thus appear to retain the extreme thermophilicity of the wild type. The quadruple mutant P10M/C11N/S235P/Q237A showed decreased thermal stability. SVD global analysis of the set of 15 spectra revealed the existence of only two species (native and unfolded), with a transition temperature of 73 °C and an enthalpy of denaturation of 35 kcal/mol. The global fit

Table 2: X-ray Data Collection and Refinement Statistics[a]

	C11N + PEP	C11N + PEP + A5P	C11N + PEP + R5P	P10M/C11N + PEP	C11N/S235P/ Q237A + PEP	C11N/S235P/ Q237A + PEP + A5P (C form)	C11N/S235P/ Q237A + PEP + A5P (D form)	P10M/C11N/ S235P/Q237A + PEP + A5P
data collection								
space group	$P3_121$	$P3_121$	$P3_121$	$P2_1$	$P2_1$	$P2_1$	$P3_121$	$P3_121$
resolution (Å)	36−1.5 (1.6−1.5)	33−1.8 (1.9−1.8)	37−1.8 (1.9−1.8)	25−2.3 (2.44−2.3)	30−2.1 (2.24−2.1)	29.8−2.1 (2.23−2.1)	25.1−1.95 (2.05−1.95)	26.1−2.0 (2.13−2.0)
unique reflections	103074 (13685)	61836 (9182)	56843 (4728)	123597 (6898)	195362 (25930)	206008 (27398)	41922 (2944)	44624 (6284)
⟨redundancy⟩	5.5 (1.6)	6.4 (3.9)	9.1 (3.1)	3.3 (1.7)	6.9 (5.0)	6.6 (5.3)	9.2 (4.4)	8.7 (5.8)
completeness (%)	97.4 (85.1)	99.7 (99.4)	88.8 (50.7)	76.3 (27.1)	91.8 (81.2)	94.9 (84.2)	86.0 (41)	98.2 (92.7)
$\langle I\rangle/\sigma\langle I\rangle$	3.9 (2.2)	3.4 (2.0)	4.1 (2.1)	8.3 (2.1)	15.6 (2.1)	6.9 (2.3)	27.5 (2.6)	7.1 (2.0)
R_{merge}[b] (%)	8.7 (26.6)	12.8 (35.0)	10.6 (35.4)	12.8 (30.6)	12.3 (35.1)	13.3 (45.8)	7.4 (32.1)	9.8 (44.3)
refinement								
PDB entry	2NWR	2NWS	2NX1	2NXI	2NXH	2NX3	2NXG	2EF9
R_{cryst}[c] (%)	22.9 (44.4)	23.4 (45.1)	20.0 (36.7)	21.0 (30.0)	20.6 (26.1)	21.6 (32.7)	21.0 (36.5)	18.8 (29.9)
R_{free} (%)	24.7 (44.7)	26.8 (45.7)	23.0 (37.8)	26.4 (35.1)	24.5 (29.3)	26.1 (35.8)	24.3 (40.1)	22.2 (31.4)
amino acids	512	525	525	3086	3128	3145	518	525
water	439	339	565	1178	1529	1624	222	402
coordinate error (Å)	0.27	0.32	0.28	0.39	0.30	0.33	0.33	0.30

[a] Each data set was collected from a single crystal at 100 K. [b] $R_{merge} = \sum_h\sum_i|I(h)_i - \langle I(h)\rangle|/\sum_h\sum_i I(h)_i$, where $I(h)_i$ is the ith measurement. [c] $R_{cryst} = \sum||F_o| - |F_c||/\sum|F_o|$. R_{free} was calculated on 10% of the data omitted from refinement. In all of the structures RMSD from ideality was determined with CNS and was not higher than 0.008 Å for bond lengths, 1.6° for bond angles, 22.9° for dihedral angles, and 0.89° for improper angles. The coordinate error was derived from a cross-validated Luzzati plot. Values in parentheses refer to the highest resolution shell.

Table 3: Chemical Denaturation of Wild-Type and Mutant KDO8PS

	ΔG_{H_2O} (kcal/mol)	m (kcal mol^{-1} M^{-1})	$[GdnHCl]_{50\%}$ (M)
KDO8PS^{WT_Cd}	3.81 ± 0.15	1.06 ± 0.04	3.61 ± 0.21
KDO8PS^{WT_Zn}	4.36 ± 0.30	1.12 ± 0.08	3.89 ± 0.40
KDO8PS$^{WT_no\ metal}$	5.56 ± 0.13	1.93 ± 0.04	2.87 ± 0.10
KDO8PS^{C11N}	8.92 ± 0.50	3.12 ± 0.17	2.86 ± 0.23
KDO8PS$^{P10M/C11N}$	4.08 ± 0.22	1.78 ± 0.09	2.30 ± 0.17
KDO8PS$^{C11N/S235P/Q237A}$	8.13 ± 0.75	3.32 ± 0.30	2.45 ± 0.32
KDO8PS$^{P10M/C11N/S235P/Q237A}$	4.89 ± 0.27	2.02 ± 0.11	2.40 ± 0.19

of the thermal denaturation data set did not improve with a model in which the enthalpy of the conformational transition was considered to be temperature dependent or with more complex models including unfolding intermediate(s).

GdnHCl denaturation curves were also obtained for the wild-type and mutant KDO8PS's. Both wild-type and mutant KDO8PS's show a single component in the equilibrium denaturation curve, suggesting that unfolding does not progress through a stable intermediate. Therefore, thermodynamic parameters associated with the denaturation curves were calculated (Table 3) from a fit to the data of a model consisting of a direct transition from folded to denatured state. Comparable values of ΔG^{H_2O}, m, and $[GdnHCl]_{50\%}$ are observed for wild-type KDO8PS in which the active site metal is either Cd^{2+} or Zn^{2+}. In contrast, the denaturation curves of metal-free wild-type KDO8PS and of the C11N and C11N/S235P/Q237A mutant proteins display changes that correspond to a smaller value of $[GdnHCl]_{50\%}$ and higher values of m (the rate at which ΔG_u changes per unit concentration of GdnHCl) and ΔG^{H_2O}. However, addition of the P10M substitution to these mutants has a destabilizing effect and brings their ΔG^{H_2O} values near wild-type levels. The larger m values of the metal-free enzymes versus the wild type suggest that in these proteins the unfolded state is more extended and solvent accessible (*25*, *33*, *34*). One possible explanation of this observation is that the metal remains bound in the denatured state and holds together distant parts of the denatured protein through its ligands.

Enzymatic Activity of the C11N Series. A mechanistic model of KDO8P synthesis that fits well both kinetic and crystallographic studies was introduced by Xu et al. (*17*) and was shown to be particularly effective in the simulation of experimental progress curves. An important feature of this model is that A5P is both a substrate (when it binds sequentially to PEP) and a dead-end inhibitor of the enzyme [when it binds independently from PEP, as shown in the structure of *A. aeolicus* KDO8PS in complex with A5P (*5*)]. In this study a modified version of Xu's model was adopted (Figure 2A) that further improved the quality of the simulations. The following features are specific to the revised model: (a) Binding of PEP to the free enzyme (Figure 2A, k_1) is considered irreversible according to a Van Slyke formalism (*35*). This change was introduced because in preliminary regression analyses the least-squares best-fit value of the off-rate constant (k_{-1}) systematically approached zero. (b) Two separate values of the off-rate constant for A5P are introduced, which refer respectively to the binding of A5P to the substrate-free enzyme (k_{-5}) and to the enzyme·PEP complex (k_{-2}). (c) A single irreversible step (Figure 2A, k_3) includes both the conversion of substrates to products and P_i release. This change was introduced because in preliminary regression analyses the best-fit value of the rate constant for the binding of P_i to the enzyme−product complex was extremely low, and conversely the best-fit value of the rate constant for the dissociation of P_i from the enzyme−product complex was extremely large. We concluded that the progress curves do not contain sufficient information to determine accurately the rate of P_i release and that this step can be considered as existing at a rapid equilibrium. (d) A step in which P_i binds also to the enzyme·PEP complex (Figure 2A, k_7 k_{-7}) was added. This step is consistent with the crystal structure of KDO8PS in complex with PEP, which shows a phosphate ion bound to the A5P binding site (*5*). Furthermore, the structure of substrate-free enzyme shows inorganic phosphate bound at the sites of the phosphate moieties of PEP and A5P (*5*). Therefore, inorganic phosphate acts as a competitive inhibitor with respect to both PEP and A5P (Figure 2A). No significant differences were observed in the magnitude of the residual between the experimental and the best-fit progress curves whether both the on- and off-rate constants were refined or only the off-rate constants. However, the smallest standard errors of the refined variables were obtained when all second-order rate constants were fixed at 10^6 s^{-1} M^{-1}. The application of these combined measures produced fits that were consistently better than those obtained using the model and parameter choice originally adopted by Xu et al. (*17*). An initial rate equation for the simplified steady-state kinetic model, corresponding to the full numerical model used in the regression analyses, was derived by application of the King−Altman method (*35*−*37*); its numerator and denominator coefficients are shown in Table 4. Kinetic constants (Table 5) were calculated by substituting the best-fit values of rate constants from our full numerical model into the rate equation according to Cleland's rules (*38*), which define k_{cat}, K_m's, and K_i's as ratios between different coefficients in the rate equation. The standard errors of the kinetic constants were calculated from the standard errors of the rate constants by error propagation (*39*). It should be noted that, since all on-rate constants (with the exception of PEP) were set at 10^{-6} s^{-1} M^{-1} in the regression analyses, most rate constants translate directly into kinetic constants (Table 5).

Analysis of Table 5 reveals similar trends in all of the enzymes of the C11N series, although the double mutant P10M/C11N behaves somewhat as an outlier. k_{cat} decreases progressively from the single to the quadruple mutant, with the latter retaining approximately 25% of the wild-type activity. K_m for PEP decreases by as much as 28 times (quadruple mutant), while the K_m and K_d for A5P increase by at most 2.6 times (double mutant). In the wild type, A5P binds more tightly to the enzyme·PEP complex (k_{-2}) than to the substrate-free enzyme (k_{-5}), and this trend is conserved in the mutants of the C11N series (compare $K_d^{A5P\_1}$ and $K_d^{A5P\_2}$).

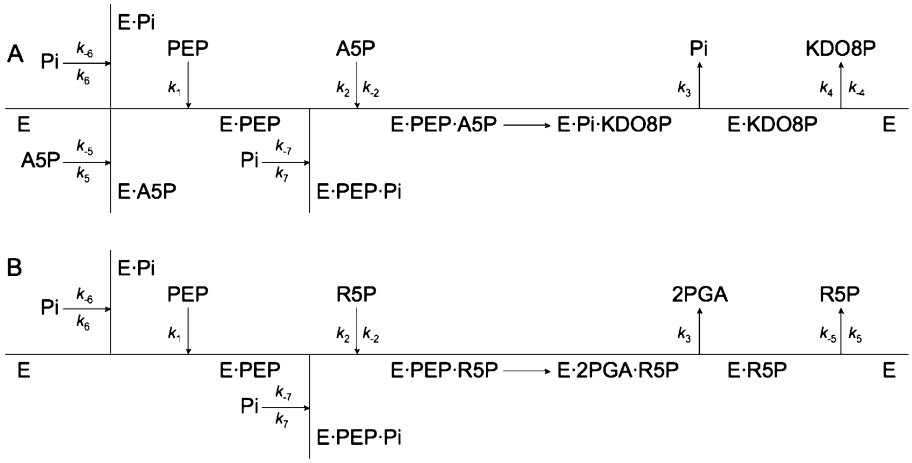

FIGURE 2: (A) Kinetic model of KDO8P synthesis. (B) Futile cycle of PEP conversion to 2-PGA in the presence of R5P (*41*). Noncovalent complexes are represented with dots.

Table 4: Rate Equation for the Kinetic Model Shown in Figure 2A

$$v = N/D$$
$$N = n_1[\mathrm{PEP}][\mathrm{A5P}]$$
$$D = d_1[\mathrm{A5P}][\mathrm{KDO8P}] + d_2[\mathrm{A5P}][\mathrm{P_i}] + d_3[\mathrm{A5P}]^2 + d_4[\mathrm{PEP}][\mathrm{P_i}] + d_5[\mathrm{PEP}][\mathrm{A5P}] + d_6[\mathrm{A5P}] + d_7[\mathrm{PEP}]$$
$$n_1 = k_1k_2k_3k_4k_{-5}k_{-6}k_{-7}$$
$$d_1 = k_2k_3k_{-4}k_{-5}k_{-6}k_{-7}$$
$$d_2 = k_2k_3k_4k_{-5}k_6k_{-7}$$
$$d_3 = k_2k_3k_4k_5k_{-6}k_{-7}$$
$$d_4 = k_1k_{-2}k_4k_{-5}k_{-6}k_7 + k_1k_3k_4k_{-5}k_{-6}k_7$$
$$d_5 = k_1k_2k_4k_{-5}k_{-6}k_{-7} + k_1k_2k_3k_{-5}k_{-6}k_{-7}$$
$$d_6 = k_2k_3k_4k_{-5}k_{-6}k_{-7}$$
$$d_7 = k_1k_{-2}k_4k_{-5}k_{-6}k_{-7} + k_1k_3k_4k_{-5}k_{-6}k_{-7}$$

The association and dissociation rate constants for KDO8P (Figure 2A, k_{-4}, k_4) define the dissociation constant K_d^{KDO8P} (Table 5). The $K_d = K_i$ for KDO8P changes significantly only in the P10M/C11N mutant (~8-fold increase). We recall here that KDO8P behaves as a product inhibitor (competitive with respect to PEP, uncompetitive with respect to A5P) (*35*). In contrast, according to the reaction scheme in Figure 2A, phosphate release from the reaction intermediate (k_3) is considered irreversible, and thus in practice P_i is not an uncompetitive product inhibitor, as might be expected for a traditional bi-bi mechanism (*35*). The dissociation constants $K_d^{P_i-1}$ and $K_d^{P_i-2}$, which refer respectively to the binding of P_i to the substrate-free enzyme and to the enzyme·PEP complex, clearly show the different nature of the P_i binding site on the substrate and product sides of the reaction. As pointed out by Xu et al. (*17*), the *A. aeolicus* enzyme exists in two different conformations at the beginning of the reaction, when P_i acts as a competitive inhibitor with respect to both PEP and A5P (Figure 2A), and upon the completion of the condensation reaction, when the binding pocket for P_i is essentially obliterated. In the wild type, P_i binds much more tightly at the PEP site ($K_d^{P_i-1}$) than at the A5P site ($K_d^{P_i-2}$). In general, in the enzymes of the C11N series binding of P_i at the PEP site is 2−7 times weaker, while binding of P_i at the A5P site is 2−3 times stronger. This fact, together with the observation that in the C11N series binding of PEP is tighter and that of A5P weaker than in the wild type, suggests that loss of the active site metal increases the enzyme affinity for the carbon moiety of PEP, while it decreases that for the carbon moiety of A5P.

E. coli KDO8PS cannot utilize ribose 5-phosphate (R5P), the epimer of A5P, as a substrate for the synthesis of KDO8P (*40*). However, in the presence of R5P this enzyme catalyzes a futile cycle in which PEP is slowly converted to 2-phosphoglycerate (2-PGA) (*41*) (Figure 2B). We have analyzed reaction progress curves recorded in the presence of R5P to determine the kinetics of the abortive PEP consumption in both the wild-type and C11N forms of *A. aeolicus* KDO8PS. R5P was used either in the presence of only PEP or in the presence of both PEP and A5P. An excellent fit to the progress curves was obtained using both reaction mechanisms described in Figure 2. This allowed the determination of the rate of 2-PGA formation (k_3^{R5P}) and the dissociation constants ($K_d^{R5P\_1}$, $K_d^{R5P\_2}$) for R5P, which are reported in Table 5. In both the wild-type enzyme and the C11N mutant, the rate constant for PEP conversion to 2-PGA in the presence of R5P is approximately 1−2% of the rate constant for the step in which PEP with A5P are used to form KDO8P. Surprisingly, R5P binds more tightly in the absence of PEP than in its presence (compare $K_d^{R5P\_1}$ and $K_d^{R5P\_2}$). This property is probably advantageous for the enzyme, as PEP binding is essentially irreversible, thus offering a good discrimination in favor of A5P during catalysis. However, R5P binds 10−20 times more tightly in C11N than in the wild type. A possible structural basis for this difference is discussed below (see the structure of the C11N mutant in complex with PEP and R5P).

Structure of C11N KDO8PS. Structures of C11N KDO8PS were determined in complex with PEP, PEP + A5P, and PEP + R5P. Crystals of C11N belong to sg $P3_121$, $a = b \approx 84$ Å and $c \approx 160$ Å, and, like the wild type, contain a dimer (half of the tetrameric enzyme) in the asymmetric unit. As noticed by Duewel et al. (*5*), the two subunits of the wild-type enzyme are slightly different, and this difference is conserved in the C11N mutant. In fact, regardless of the type of ligand bound, RMS deviations are significantly smaller between the mutant A and wild-type A subunit and between the mutant B and wild-type B subunit than between mutant A and wild-type B or between mutant B and wild-type A. Crystals of C11N in complex with PEP diffract to high resolution (1.5 Å) and offer a unique opportunity to examine the structure of this mutant in very high detail. The overall features of the protein are conserved in C11N, with key differences appearing only around the replacement position. Although C11N crystals were incubated in the presence of 50 μM $CdCl_2$ (as in all previous studies of the wild-type

Table 5: Kinetic and Rate Constants for KDO8P Synthesis in Wild Type and in Enzymes of the C11N Series[a]

rate eq coeff/ rate constants	kinetic constants	WT	C11N	P10M/C11N	C11N/S235P/ Q237A	P10M/C11N/ S235P/Q237A
N1/D5	k_{cat}	0.47 ± 0.02	0.18 ± 0.008	0.22 ± 0.02	0.16 ± 0.01	0.11 ± 0.01
k_3		0.58 ± 0.002	0.19 ± 2e-4	0.22 ± 1e-4	0.17 ± 4e-4	0.12 ± 1e-4
k_3^{R5P}		0.01 ± 0.002	0.002 ± 6e-5			
D6/D5	K_m^{PEP}	0.13 ± 0.004	0.01 ± 5e-4	0.03 ± 2e-3	0.008 ± 5e-4	0.005 ± 5e-4
D7/D5	K_m^{A5P}	2.75 ± 0.09	6.78 ± 0.28	7.28 ± 0.68	6.82 ± 0.44	5.13 ± 0.54
$k_{-2}/k_2 = k_{-2}$	$K_d^{A5P\_1}$	2.87 ± 0.03	7.00 ± 0.03	7.15 ± 0.07	7.05 ± 0.04	5.10 ± 0.05
$k_{-2}^{R5P}/k_2^{R5P} = k_{-2}^{R5P}$	$K_d^{R5P\_1}$	176.9 ± 19.37	7.03 ± 0.18			
$k_4/k_{-4} = k_4$	K_d^{KDO8P}	2.27 ± 0.03	3.07 ± 0.05	17.20 ± 0.64	2.87 ± 0.10	6.56 ± 0.44
$k_{-5}/k_5 = k_{-5}$	$K_d^{A5P\_2}$	15.72 ± 0.23	5.44 ± 0.09	43.53 ± 1.50	17.00 ± 0.35	14.18 ± 0.24
$k_{-5}^{R5P}/k_5^{R5P} = k_{-5}^{R5P}$	$K_d^{R5P\_2}$	0.27 ± 0.02	0.02 ± 0.001			
$k_{-6}/k_6 = k_{-6}$	$K_d^{Pi\_1}$	9.04 ± 0.11	23.03 ± 0.31	69.85 ± 1.70	57.85 ± 1.40	16.99 ± 0.37
$k_{-7}/k_7 = k_{-7}$	$K_d^{Pi\_2}$	383.4 ± 3.92	130.3 ± 0.61	110.2 ± 1.20	141.2 ± 0.96	161.0 ± 1.70
$N1/D6 = k_1$	k_{cat}/K_m^{PEP}	3.61 ± 0.18	15.25 ± 0.88	8.27 ± 1.07	21.37 ± 1.98	24.83 ± 3.71
N1/D7	k_{cat}/K_m^{A5P}	0.17 ± 0.008	0.03 ± 0.002	0.03 ± 0.004	0.02 ± 0.002	0.02 ± 0.003

[a] k_{cat}, k_3, and k_3^{R5P} are in units of s^{-1}, and k_{cat}/K_m is in units of s^{-1} μM^{-1}; all other kinetic constants are in units of μM.

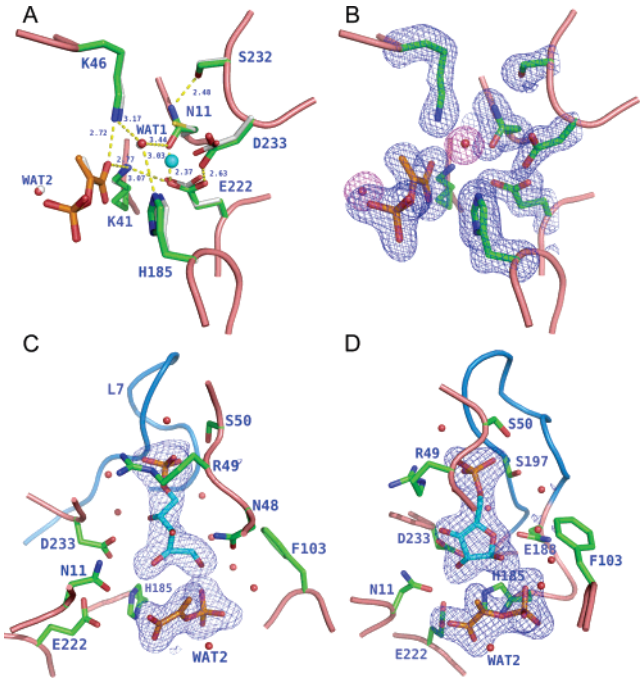

FIGURE 3: (A) C11N mutant in complex with PEP. A network of hydrogen bonds surrounds a water molecule (WAT1) situated on the *si* side of $C2^{PEP}$ (shown here with orange bonds). Another water molecule (WAT2) is situated on the *re* side of $C2^{PEP}$. The superposed structure of the wild-type enzyme is shown with white bonds/spheres. The position of the active site metal in the wild type is marked by a cyan sphere. Hydrogen bonds are shown as dashed lines, with the bond length in Å. (B) Same view as (A) but showing only C11N and the electron density map of the region. (C) C11N mutant in complex with PEP (orange bonds) and A5P (cyan bonds). A5P displaces WAT1. The distance between $C3^{PEP}$ and $C1^{A5P}$ is 3.6 Å. The L7 loop (light blue) is closed. (D) C11N mutant in complex with PEP (orange bonds) and R5P (cyan bonds). R5P is bound in its cyclic form; the L7 loop (light blue) is closed. The electron density maps shown in panels B, C, and D are $|F_o - F_c|$ σA omit maps contoured at 3σ. Hydrogen bonds are shown as dashed yellow lines with distances (Å) in blue. Water molecules are shown as red (C11N) or white (wild-type) spheres.

enzyme), no metal is visible in the active site (Figure 3A,B), which therefore resembles the active site of the *E. coli* enzyme. The carboxamide moiety of Asn-11 is almost parallel to the carboxylate moiety of Asp-233 and approximately perpendicular to the carboxylate moiety of Glu-222; there is a strong hydrogen bond between the OD1 oxygen (or ND2 nitrogen) of Asn-11 and one of the two carboxylate oxygens of Glu-222. Also in hydrogen bond range of the carboxamide moiety of Asn-11 are the OG of Ser-232 and a water molecule located on the *si* side of PEP (Figure 3A, WAT1). WAT1 occupies the same position as the water bound to the active site metal of wild-type KDO8PS. As in the wild type, a water molecule is also present on the *re* side of PEP (Figure 3A, WAT2). WAT1 and WAT2 are both well positioned for a nucleophilic attack on $C2^{PEP}$, although WAT2 is closer to PEP than WAT1 (Table 6). Altogether, the positions of the active site residues are almost identical in the wild type and in C11N, with the most significant displacements observed in the carboxylate moiety of Asp-233. As observed in the structure of wild-type KDO8PS (*5*), as well as in the homologous DAH7PS (*42*, *43*), the plane of the carboxylate moiety of PEP is rotated around the C1−C2 bond by almost 30° with respect to the enol plane, defined by C1, C3, and the phosphate bridging O atom. The L7 loop is not ordered.

The structure of the C11N mutant in complex with PEP and A5P was determined at the resolution of 1.8 Å. PEP and A5P bind in both active sites contained in the asymmetric unit (Figure 3C); the density for A5P is among the clearest ever observed for this enzyme. The L7 loop is ordered and closed in both active sites. This is very different from the wild type, in which one active site contains PEP and A5P while the other contains only PEP (*5*). In the wild-type enzyme the L7 loop is in a closed conformation in the active site in which both substrates bind and disordered in the active site in which only PEP binds. Another feature of the C11N enzyme is that A5P binds in a different orientation with respect to the wild type (Figure 3C), such that $C2\text{-}OH^{A5P}$ displaces the water molecule located on the *si* side of $C2^{PEP}$ (WAT1). The water molecule located on the *re* side of $C2^{PEP}$ (WAT2) is conserved (see also Table 6).

In the wild-type enzyme ribose 5-phosphate (R5P) binds to only one of the two subunits in the asymmetric unit, and there it displaces WAT1. The fact the R5P, despite being the epimer of A5P, is not capable of driving the synthesis of KDO8P has been attributed to the loss of this water molecule (*6*). For this reason it was of interest to determine whether R5P produces a similar effect in the C11N mutant. The structure of the mutant enzyme in complex with PEP and R5P was determined at the resolution of 1.8 Å; as with A5P, R5P binds in both subunits of the asymmetric unit and

Table 6: Distances (Å) between WAT1 or WAT2 and $C2^{PEP}$ or $C2^{INT}$ in Different Subunits of the C11N Series Mutants

	C11N + PEP		C11N + PEP + A5P		P10M/ C11M + PEP		C11M/S235P/ Q237A + PEP		C11M/S235P/ Q237A + PEP + A5P (C form)		C11M/S235P Q237A + PEP + A5P (D form)		P10M/C11M/ S235P/ Q237A + PEP + A5P		wild type + PEP		wild type + PEP + A5P	
	WAT1	WAT2	WAT1	WAT2	WAT1	WAT2	WAT1	WAT2	WAT1	WAT2	WAT1	WAT2	WAT1	WAT2	WAT1	WAT2	WAT1	WAT2
A	3.67	3.17	–	3.01	–	–	3.59	3.07	–	2.75	–	3.11	–	2.97	3.49	3.15	3.43	3.19
B	3.69	3.15	–	3.00	3.60	–	3.68	2.95	–	2.72	–	3.66[a]	–	3.02	3.55	3.21	3.35	3.18
C					3.75	–	3.74	3.12	–	2.94								
D					–	–	3.69	3.10	–	–[a]								
E					–	–	–	–	–	–								
F					–	–	–	3.13	–	3.16								
G					3.58	–	3.59	3.03	–	2.80								
H					3.71	2.98	3.65	3.14	–	2.79								
I					3.37	2.83	3.66	3.06	–	2.79								
J					–	–	3.66	3.13	–	2.80								
K					–	–	3.49	3.18	–	3.06								
L					–	–	3.63	3.22	–	–								

[a] The reaction intermediate is present in this active site.

displaces WAT1. Furthermore, in both active site the L7 loop is ordered and closed. A second key difference with respect to the wild type is that R5P binds in its cyclic furanose form (Figure 3D). This unusual affinity for the cyclic form of R5P, expected to be the prevalent form of the sugar in solution, may represent the physical basis for the much smaller value of K_d^{R5P} observed in C11N with respect to the wild-type enzyme (see Table 5). Also worth noting is the fact that in this structure the carboxylate moiety of PEP is rotated by as much as 35° with respect to the enol plane. This is one of the largest deviations of PEP from planarity observed in all structures of KDO8PS.

Structure of the Double Mutant P10M/C11N. Crystals of the P10M/C11N mutant were obtained in the absence of substrate. No diffraction beyond 5 Å was observed when these crystals were soaked with PEP and A5P. However, a data set was collected at the resolution limit of 2.3 Å from a crystal soaked with only PEP (5 mM) (sg $P2_1$, a = 75.9 Å, b = 197.5 Å, c = 124.9 Å, β = 93.8°; Table 2). There are three complete tetramers in the asymmetric unit. The overall architecture of P10M/C11N is very similar to that of the wild type, with only a few differences among the 12 subunits of the enzyme contained in the asymmetric unit. As seen in C11N, replacement of Cys-11 with Asn is easily accommodated in the active site cavity. In contrast, replacement of Pro-10 with Met perturbs the region comprising residues 15−22 (end of the L1 loop and beginning of the H1 helix), with the largest displacement observed at Leu-18 and Leu-19. This shift extends in part to the following H1 helix. The L7 loop is closed in 2 subunits but is disordered in the other 10. In 5 out of 12 subunits PEP binds also at the A5P binding site. In the PEP molecule bound at the standard site of the P10M/C11N enzyme the extent of the rotation of the carboxylate moiety with respect to the enol plane ranges in different subunits from a few degrees to 20−30°. In addition to this rotation, in some subunits the phosphate atom, which normally also sits approximately in the enol plane, is slightly displaced outside of this plane, in the direction of the *si* side of PEP. In two subunits, two water molecules are located respectively on the *si* and *re* sideof $C2^{PEP}$ (Table 6). In most of the other subunits no water is visible on either side of PEP. The conformation of PEP bound at the A5P site appears to be different from that observed at the primary site, with the plane of the carboxylate moiety in some cases almost perpendicular to the enol plane. The physiological significance of PEP binding also at the A5P site in this structure is not clear.

Structure of the Triple Mutant C11N/S235P/Q237A. Among the residues lining the active site cavity that are different in metallo and nonmetallo KDO8PS's, two belong to the L8 loop. In the *A. aeolicus* enzyme these are Ser-235 (proline in *E. coli*) and Gln-237 (alanine in *E. coli*) (Table 1) (Figure 4). The triple mutant C11N/S235P/Q237A was crystallized in the substrate-free form (form A: sg $P3_1$-21, $a = b$ = 83.92 Å, c = 160.62 Å), with PEP bound (form B: sg $P2_1$, a = 76.21 Å, b = 198.63 Å, c = 125.52 Å, β = 94.28°), and with PEP + A5P (form C: sg $P2_1$, a = 76.38 Å, b = 198.53 Å, c = 125.83 Å, β = 94.19°). An alternative form of the enzyme in complex with both PEP and A5P (form D: sg $P3_121$, $a = b$ = 84.15 Å, c = 160.65 Å) was obtained by soaking crystals of the substrate-free enzyme in the presence of both substrates.

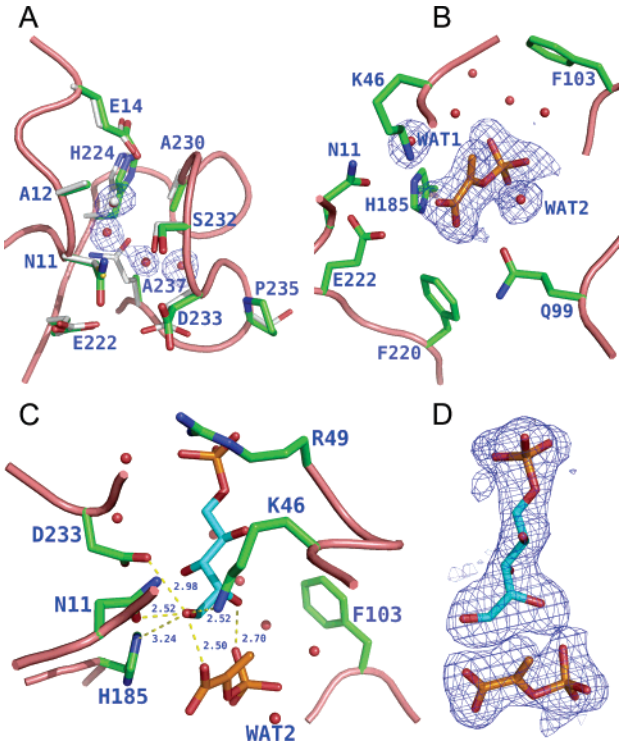

FIGURE 4: Structure of the C11N/S235P/Q237A mutant enzyme. (A) Crystal form B: the three mutations are packed in a very small space wrapped by the L8 loop (residues 225−240). The structure of the mutant enzyme (green bonds) is superimposed to the wild type (white bonds). Two water molecules fill the cavity produced by the Q237A substitution. (B) Crystal form B (complex with PEP): active site of 1 of the 12 subunits contained in the asymmetric unit with an $|F_o - F_c|$ σA omit map contoured at 3σ around PEP (orange bonds), WAT1, and WAT2. (C) Crystal form C (complex with PEP + A5P): active site of 1 of the 12 subunits contained in the asymmetric unit. PEP is shown with orange bonds and A5P with cyan bonds. Hydrogen bonds are shown as dashed yellow lines, with the bond length (Å) in blue. The distance between $C3^{PEP}$ and $C1^{A5P}$ is 2.9 Å. (D) Detail of the same active site showing an $|F_o - F_c|$ σA omit map contoured at 3σ around PEP and A5P.

Crystals of the B form (sg $P2_1$: enzyme in complex with PEP) contain three tetramers in the asymmetric unit, for a total mass of 360 kDa. A unified picture of the C11N/S235P/Q237A enzyme emerges from their analysis. The overall structure of the triple mutant is very similar to that of the wild-type enzyme, with the exception of a few compensatory changes directed at filling the cavity produced by the Q237A substitution. The side chain of Gln-237 is replaced by two water molecules (Figure 4A), and the L8 loop and H8 helix are slightly shifted. The structural perturbations emanating from the mutation site extend to helix H7 on one side and helices H1 and H2 on the other side of H8 (not shown). The dynamics of the nearby L7 loop are also affected, as in 2 out of 12 subunits, this loop is closed, despite the fact that only PEP is present in the crystal. The geometry of PEP at the C2 center ranges in different subunits from planar to twisted with significant degrees of rotation of the carboxylate moiety with respect to the enol plane. In some subunits the carboxylate and enol planes are approximately coplanar, but the phosphate moiety is significantly shifted toward the *si* side of the enol plane. In most subunits a water molecule is present on both sides of $C2^{PEP}$ (Figure 4B). As observed in the structure of the wild-type enzyme, WAT2 (*re* side of PEP) is always closer to $C2^{PEP}$ than WAT1 (*si* side of PEP) (Table 6).

Although obtained under different conditions, the C (sg $P2_1$, crystallized with PEP and A5P) and D forms (sg $P3_1$-21, substrate-free crystals soaked with PEP and A5P) of the C11N/S235P/Q237A crystals give a similar picture of the mutant enzyme in complex with both substrates. As described for the B form, also in the C form there are three tetramers in the asymmetric unit. PEP and A5P are bound in 9 out of 12 subunits, and the L7 loop is closed in 10 out of 12 subunits. Thus, also in this mutant, as already noted for C11N, there is a loss of the structural asymmetry characteristic of the wild type, which would manifest itself as PEP and A5P binding together only in 6 out of 12 subunits (*5*). Of particular note is the fact that in all of the subunits in which A5P binds its conformation is different from that observed in the wild type (Figure 4C,D). The aldehyde carbonyl of A5P completely displaces the water molecule on the *si* side of PEP and is in hydrogen bond distance of the carboxamide moiety of Asn-11, the carboxylate moiety of Asp-233, and the carboxylate moiety of PEP. At the same time $C2\text{-}OH^{A5P}$ is in hydrogen bond distance of one of PEP phosphate hydroxyls. The positive charges of Lys-46 and His-185 are near the A5P carbonyl. This spatial arrangement of the active site side chains creates an interesting situation in which the carbonyl oxygen of A5P occupies a narrow channel between two negative charges (respectively on the *si* and *re* side of $C1^{A5P}$) and two positive charges located on a plane almost perpendicular to that harboring the negative charges. The carboxamide moiety of Asn-11 is located at the end of the channel. Although the overall pattern of hydrogen bonds is the same in 11 out of 12 subunits (see below for the exception), there is significant variation between the different subunits in the distances separating the carbonyl oxygen of A5P from its hydrogen bond partners. In 4 subunits the electron density of PEP is not well defined at C3. In 3 out of 12 subunits, $C2^{PEP}$ shows a pseudotetrahedral configuration, although the electron density map does not reveal the presence of a C2 hydroxyl as it would occur if PEP had converted to a hydroxylated tetrahedral intermediate. In general, in the subunits in which there is significant deviation from planarity at $C2^{PEP}$ the carbonyl of A5P is closer to the amine of Lys-46. Instead, when $C2^{PEP}$ is more clearly planar, the A5P carbonyl is closer to Asn-11 and Asp-233 and more distant from Lys-46 and the PEP carboxylate. In 9 out of 12 subunits, a water molecule is clearly visible on the *re* side of PEP.

The reaction intermediate is visible in the active site of 1 of the 12 subunits of the C form and of 1 of the 2 subunits of the D form (Figure 5). This is the first direct observation of this intermediate in a crystal structure and confirms earlier identification of this chemical species by electrospray ionization mass spectrometry (*4*). In the C form the electron density of the intermediate is not very well defined (Figure 5A), and thus there is some ambiguity with regard to the configuration of the C2 chiral center. In the D form, the electron density is of very good quality (Figure 5C), and we were able to define the chemical nature of the intermediate in a quantitative and unbiased way, as described below. According to the mechanism postulated in path A of Figure 1, the reaction intermediate can have only one configuration, originating from attack by a metal-activated water (WAT1) on the *si*

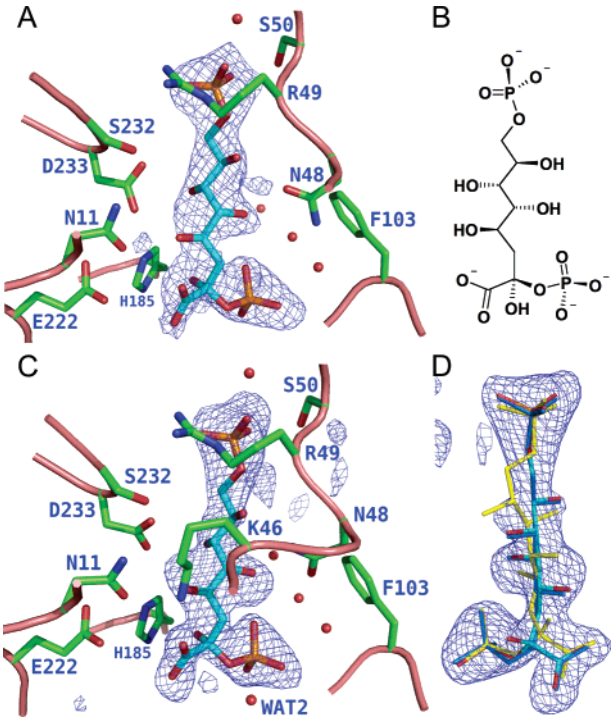

FIGURE 5: C11N/S235P/Q237A mutant: structure of the reaction intermediate. (A) Crystal form C: active site of 1 of the 12 subunits contained in the asymmetric unit. (B) Anticipated chemical structure of INT if water attacks the *si* side of $C2^{PEP}$ or $C2^{OXO}$. (C) Crystal form D: active site of 1 of the 2 subunits contained in the asymmetric unit. (D) Detail of the active site shown in (C), but rotated by approximately 180° around the vertical axis, showing three alternative interpretations of the electron density: INT produced by water attack from the *si* side (cyan) or the *re* side (yellow) and OXO (dark blue). In panels A and C an $|F_o - F_c|$ σA omit electron density map is contoured at 3σ around INT (cyan bonds) produced by water attack from the *si* side (as in panel B), shown here as the best fit to the electron density.

side of $C2^{PEP}$ (*6*). In principle, according to the mechanism postulated in path B of Figure 1, water addition can occur from either side of the oxocarbenium (OXO) ion (*10*, *18*). However, in practice, water addition is expected to occur either only from the *si* side or only from the *re* side of $C2^{PEP}$. On this basis, it was of interest to determine whether the electron density observed in the active site of the triple mutant C11N/S235P/Q237A is better accounted for by (a) INT produced by water attack from the *si* side of C2 (path A or B), (b) INT produced by water attack from the *re* side of C2 (path B), or (c) OXO (path B). For this purpose, the D form of the C11N/S235P/Q237A structure, which has the highest resolution and the best quality maps, was refined in separate rounds by incorporating in the topology database each of the three possible chemical forms of the intermediate. Then the real-space *R* factor was calculated for the model of the intermediate used in each refinement against an $|F_o - F_c|$ σA omit map of the region of the active site occupied by the intermediate. The best fit was obtained with a chemical model of INT (Figure 5B,D), in which water was added from the *si* side of $C2^{PEP}$ or of $C2^{OXO}$ (real space $R =$ 0.096). Poorer fits were obtained with a model of INT in which water has attacked from the *re* side (real space $R =$ 0.108) or with a model of OXO (real space $R = 0.119$) (Figure 5D). Furthermore, in the structure of the D form a small protuberance can be recognized in the electron density of the intermediate at the position where a C2-hydroxyl group would reside if water had attacked from the *si* side of $C2^{PEP}$ or of $C2^{OXO}$ (Figure 6). In the D form a water molecule is clearly visible near the intermediate, in the position corresponding to the *re* side of PEP (WAT2), suggesting that this water is not used in the condensation reaction. In the C form the L7 loop is closed and traps the intermediate, while in the D form it is disordered, perhaps representing a later step in catalysis in which the active site opens to allow product release. In the other active site of the D form PEP and A5P have not undergone condensation, and the L7 loop is closed. In this active site A5P adopts the conformation observed in the wild-type enzyme, with the aldehyde carbonyl close to the phosphate moiety of PEP. A water molecule is visible only on the *re* side of PEP, which, as observed in other structures, displays significant rotation (~20°) of the carboxylate moiety with respect to the enol plane.

Structure of the Quadruple Mutant P10M/C11N/S235P/Q237A. Crystals of the quadruple mutant P10M/C11N/S235P/Q237A were obtained only in the absence of added substrate. These crystals diffract very poorly (~20 Å), and the diffraction limit is not extended by addition of 5 mM PEP. However, incubation of the crystals for 1 day in a holding solution containing 5 mM PEP and 5 mM A5P improved the diffraction, and a data set (sg $P3_121$: $a = b =$ 84.57 Å, $c = 159.7$ Å) was collected at the resolution limit of 2.0 Å. The structure of P10M/C11N/S235P/Q237A is similar to that of the simpler mutant C11N. Both subunits contained in the asymmetric unit bind PEP and A5P. In particular, in each active site A5P adopts the conformation in which the aldehyde carbonyl is near the phosphate moiety of PEP. In both subunits a water molecule is visible only on the *re* side of PEP, which displays the usual rotation (10−20°) of the carboxylate moiety of PEP with respect to the enol plane. In both subunits, the L7 loop is closed. Other parts of the structure show a combination of the perturbations observed in the double mutant P10M/C11N and in the triple mutant C11N/S235/Q237. However, the helix shifts observed in the triple mutant are barely noticeable in the quadruple mutant.

DISCUSSION

The structures of the C11N, P10M/C11N, C11N/S235P/Q237A, and P10M/C11N/S235P/Q237A variants of *A. aeolicus* KDO8PS were determined from crystals maintained in the presence of 50 μM Cd^{2+}, a concentration sufficient to ensure metal binding in the active site of the wild-type enzyme (*5*). However, no metal ion is visible in the active site of the C11N series, confirming earlier biochemical observations (*20*−*22*) that the single C11N substitution is capable of converting a metallo KDO8PS into its nonmetallo counterpart. Despite the absence of metal, the enzymes of the C11N series still bind both PEP and A5P and thus provide a first high-resolution glimpse of the active site of a nonmetallo KDO8PS with bound substrates. The structures reveal important functional differences between metallo and nonmetallo KDO8PS's. First, PEP and A5P bind in all of the active sites of these engineered nonmetallo enzymes, and the L7 loop is closed in these sites. This is in stark contrast with the (metallo) wild-type enzyme, in which the active sites on one face of the enzyme contain PEP and A5P, while the active sites on the other face contain PEP and P_i (*5*). Also, in the wild-type enzyme the L7 loop is in a closed

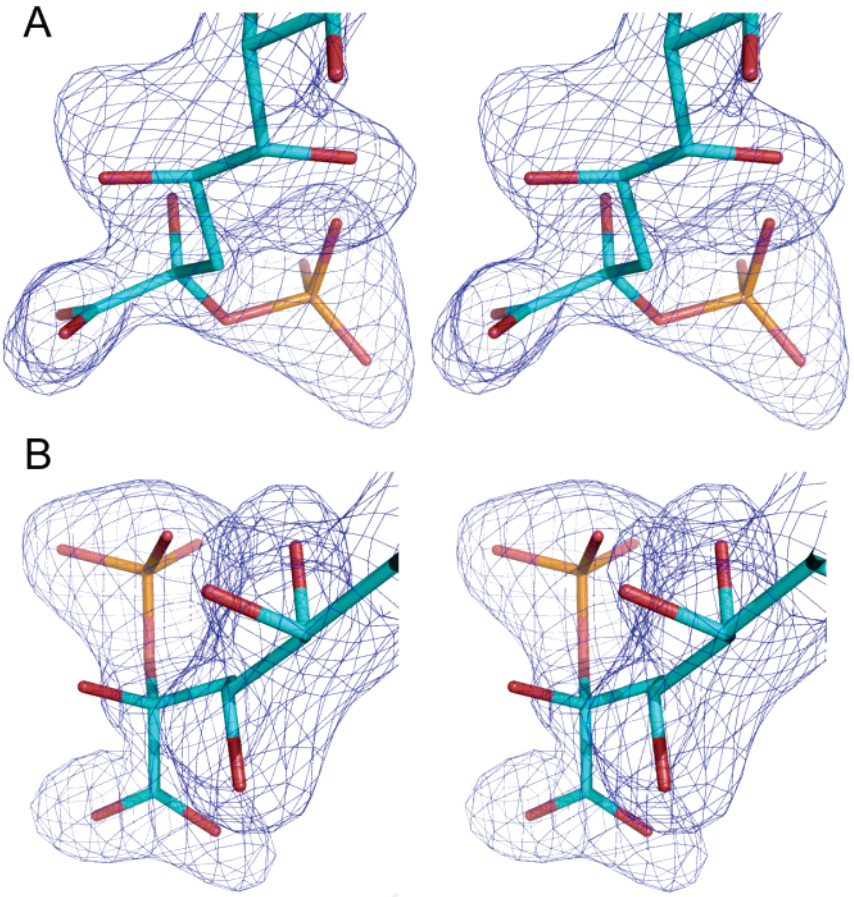

FIGURE 6: Stereoview of the $|F_o - F_c|$ σA omit map contoured at 3σ around INT in the crystal form D of C11N/S235P/Q237A. Panels A and B are different orientations of the same molecule aimed at showing, respectively, that the C2 center (half way between the carboxylate and phosphate moieties) is not planar and that a small protuberance of the electron density engulfs, albeit not completely, the C2 hydroxyl.

conformation in the active sites in which both substrates bind and is disordered in the active sites in which only PEP binds. However, if the wild-type enzyme is treated with EDTA, and the metal is removed from the active site, then PEP and A5P bind in both faces of the enzyme (*5*). Notably, under these conditions the L7 loop becomes ordered and assumes a closed conformation in all four active sites of the tetramer (*5*). Thus, loss of the metal by either chelation or mutation (e.g., the C11N series) eliminates the structural asymmetry between the two faces of the enzyme. Another common feature of the enzymes of the C11N series is that A5P displaces the water molecule (WAT1) located on the *si* side of $C2^{PEP}$ (Figures 3C and 4C). The water molecule located on the *re* side of $C2^{PEP}$ (WAT2) is always conserved. However, if only PEP is added to the crystals, both WAT1 and WAT2 are present (Figures 3AB and 4B). Two conformations of A5P are observed in the C11 series, which are related by a rotation of 180° around the long axis of A5P. In C11N and P10M/C11N/S235P/Q237A WAT1 is displaced by $C2\text{-}OH^{A5P}$ (conformation A, Figure 3C). In C11N/S235P/Q237A WAT1 is displaced by the aldehyde carbonyl ($O1^{A5P}$) (conformation B, Figure 4CD). Conformation B is of particular interest because it places the A5P carbonyl in a narrow cavity defined by the carboxamide moiety of Asn-11 and by two negative charges (the carboxylate moieties of Asp-233 and PEP) situated in a plane perpendicular to that of two positive charges (the amines of Lys-46 and His-185). This particular spatial distribution of charges may have an orienting effect on the $O1^{A5P}$ orbital that would harbor the incipient negative charge on this oxygen during the condensation step and, thus, favor the capture of a proton from either Lys-46 or His-185. The B conformation is likely to represent the catalytically competent conformation of A5P. This is suggested by the fact that in this conformation both the carbonyl oxygen and all of the hydroxyl groups of A5P are in the same positions that they assume in INT, visualized here for the first time in the structures of the C11N/S235P/Q237A mutant (Figure 5). Furthermore, in this conformation the distance between $C3^{PEP}$ and $C1^{A5P}$ (2.9 Å) is significantly shorter than in the A conformation (3.6 Å), which might favor the formation of a bond between these atoms. The fact that INT is clearly visible in some of the active sites of the mutant enzyme is remarkable in itself, as both chemical considerations and experimental studies (*4*) suggest that this chemical species is highly unstable. Careful inspection of the electron density shape and quantitative analysis of the real-space *R* factors of different possible chemical models suggest that this intermediate is likely to originate from water attack on the *si* side of $C2^{PEP}$ or $C2^{OXO}$ (Figures 5D and 6). This conclusion is difficult to reconcile with the observation that, in all of the structures of the C11N series in which both PEP and A5P are bound, only a water molecule on the *re* side of PEP (WAT2) is visible (Figures 3 and 4). However, it is important to stress that, as *A. aeolicus* KDO8PS is a hyperthermophilic enzyme, there is negligible enzymatic activity in the crystals, which are stable only at 4 °C. Both the low temperature at which the crystals are maintained and an alteration of the

energy barriers along the reaction coordinate must contribute to the unprecedented stability of INT in some of the subunits of the triple mutant. The issue of stabilization of intermediates in the active site of KDO8PS is of particular relevance here. For example, a water molecule on the *si* side of PEP might react at C2 forming the tetrahedral carbanionic species at C3 postulated in path A of Figure 1. If this intermediate is sufficiently stable, its life span will encompass a subsequent A5P binding (in the position shown in Figure 4A) that will trigger the condensation reaction. However, this intermediate is expected to be highly basic ($pK_a \sim 30$), with no resonance stabilization and to rapidly decompose by abstracting a proton from water or from a surrounding residue (*22*). Thus, if A5P binds and displaces WAT1 before it reacts with PEP or if the hydroxylated derivative of PEP decays before A5P binds, then a situation will emerge that is comparable to that recorded in most of the active sites of the triple mutant, in which WAT1 is absent and A5P sits near PEP but cannot start a condensation reaction because the hydroxylated intermediate of PEP was not formed or decayed at an earlier stage. Alternatively, the first step of the condensation reaction might be the formation of OXO as postulated by path B of Figure 1, starting from relative positions of the two substrates similar to those shown in Figure 4A. If OXO is sufficiently stable, a water molecule could then come in from the bulk phase and attack on the *si* side of $C2^{OXO}$.

Of all the mutations studied, P10M seems to be the only one that does not fit nicely in a path of conversion from metallo to nonmetallo KDO8PS. For example, introduction of P10M into the background of the triple mutant brings the enzyme closer to the phenotype observed in C11N. Furthermore, the P10M substitution has a destabilizing effect, as attested by the decrease in the free energy of unfolding of P10M/C11N with respect to C11N and of P10M/C11N/S235P/Q237A with respect to C11N/S235P/Q237A (Table 3). The quadruple mutant is also the enzyme of the C11N series with the lowest activity (Table 5) and the lowest stability to thermal denaturation. In this context, it is important to note that the presence of Pro before Asn in KDO8PS's from higher plants (*11*, *44*) suggests that methionine is not mandatory at this position for nonmetallo catalysis. Altogether, these observations suggest that P10M/C11N and P10M/C11N/S235P/Q237A are not on a direct path between metallo and nonmetallo KDO8PS's.

The reason for the existence of two classes of KDO8P synthases, one with and one without metal, remains elusive. It has been argued that the metal of KDO8PS and of the homologous enzyme DAH7PS is not involved in catalysis but serves only a structural function (*10*). However, the free energy of unfolding in water of wild-type KDO8PS deprived of the active site metal, or of engineered forms of KDO8PS lacking the metal binding Cys-11, is actually larger than that of the metalloenzyme (Table 3). Furthermore, the electron density map of the reaction intermediate observed in the structures of the triple mutant (Figure 5) is consistent with an attack by a water molecule located on the *si* side of PEP. Most likely, this would be the water molecule that is directly coordinated to the active site metal in metallo KDO8PS or hydrogen bonded to the carboxamide moiety of Asn-11 in nonmetallo KDO8PS. It is probably not fortuitous that Asn is the only residue that throughout the evolution of KDO8PS has proven capable of replacing the combination Cys-Me^{2+} (*20*, *21*). On this basis, it is tempting to speculate that the *si* side of PEP represents a "hot" area of both metallo and nonmetallo KDO8PS's and that in both classes of enzymes activation of a water molecule at this site is favored by a combination of factors like the distortion of PEP, a particular coordination geometry of the active site metal, or the orientation and hydrogen bonding of the carboxamide moiety of an Asn residue. Further investigation by computational means of how the shape and charge distribution of the active site might produce this favorable electronic structure is undoubtedly necessary.

In the wild-type enzyme, the carboxylate moiety of PEP and the aldehyde moiety of A5P (or R5P) are in close proximity of the outer coordination shell of the metal, and thus, regardless of whether a metal is directly involved in catalysis or not, its presence (or absence) in the active site of KDO8PS affects the binding properties of both substrates. In all of the enzymes of the C11N series K_m^{PEP} is smaller and K_m^{A5P} is larger (Table 5). The K_d's for P_i and R5P, two abundant compounds in the cell cytoplasm, which act as competitive inhibitors of KDO8PS, are also changed. In this context it is important to remember that the engineered forms of nonmetallo KDO8PS simply mimic the naturally occurring variants of these enzymes and that the changes in kinetic and binding parameters that are observed in the enzymes of the C11N series might not be a degradation of the original function but rather the expression of a different one. In fact, an additional role for the metal in the active site of KDO8PS might be to modulate the binding properties of ligands in response to environmental changes. Very little is known about the actual concentrations of metabolites like PEP, A5P, R5P, or even phosphate in vivo in different bacteria. Significant variations in the concentrations of these compounds across the bacterial kingdom might have been another factor that drove the evolution of two classes of KDO8P synthases. Thus, it is entirely possible that the presence or lack thereof of the active site metal in KDO8PS may simply reflect an adaptation of the enzyme to different cellular milieus, without having to modify in a more drastic way the core catalytic mechanism.

ACKNOWLEDGMENT

We thank Dr. Sharon Ackerman for critical evaluation of the manuscript.

SUPPORTING INFORMATION AVAILABLE

Thermal denaturation of the enzymes of the C11N series, chemical denaturation of the enzymes of the C11N series, kinetic analysis of the enzymes of the C11N series, structure of P10M/C11N in complex with PEP, structure of C11N/S235P/Q237A in complex with PEP, and structural variation between subunits in the enzymes of the C11N series. This material is available free of charge via the Internet at http://pubs.acs.org.

REFERENCES

1. Raetz, C. R., and Whitfield, C. (2002) Lipopolysaccharide endotoxins, *Annu. Rev. Biochem. 71*, 635−700.
2. Raetz, C. R. (1990) Biochemistry of endotoxins, *Annu. Rev. Biochem. 59*, 129−170.

3. Levin, D. H., and Racker, E. (1959) Condensation of arabinose 5-phosphate and phosphorylenol pyruvate by 2-keto-3-deoxy-phosphooctonic acid synthetase, *J. Biol. Chem. 234*, 2532−2539.
4. Li, Z., Sau, A. K., Shen, S., Whitehouse, C., Baasov, T., and Anderson, K. S. (2003) A snapshot of enzyme catalysis using electrospray ionization mass spectrometry, *J. Am. Chem. Soc. 125*, 9938−9939.
5. Duewel, H. S., Radaev, S., Wang, J., Woodard, R. W., and Gatti, D. L. (2001) Substrate and metal complexes of 3-deoxy-D-*manno*-octulosonate 8-phosphate synthase from *Aquifex aeolicus* at 19 Å resolution: implications for the condensation mechanism, *J. Biol. Chem. 276*, 8393−8402.
6. Wang, J., Duewel, H. S., Woodard, R. W., and Gatti, D. L. (2001) Structures of *Aquifex aeolicus* KDO8P synthase in complex with R5P and PEP, and with a bisubstrate inhibitor: role of active site water in catalysis, *Biochemistry 40*, 15676−15683.
7. Kohen, A., Berkovich, R., Belakhov, V., and Baasov, T. (1993) Stereochemistry of KDO8P synthase. An efficient synthesis of the 3-fluoro analogs of KDO8P, *Bioorg. Med. Chem. Lett. 3*, 1577−1582.
8. Dotson, G. D., Dua, R. K., Clemens, J. C., Wooten, E. W., and Woodard, R. W. (1995) Overproduction and one-step purification of *Escherichia coli* 3-deoxy-D-*manno*-octulosonic acid 8-phosphate synthase and oxygen transfer studies during catalysis using isotopic-shifted heteronuclear NMR, *J. Biol. Chem. 270*, 13698−13705.
9. Dotson, G. D., Nanjappan, P., Reily, M. D., and Woodard, R. W. (1993) Stereochemistry of 3-deoxyoctulosonate 8-phosphate synthase, *Biochemistry 32*, 12392−12397.
10. Furdui, C., Zhou, L., Woodard, R. W., and Anderson, K. S. (2004) Insights into the mechanism of 3-deoxy-D-*arabino*-heptulosonate 7-phosphate synthase (Phe) from *Escherichia coli* using a transient kinetic analysis, *J. Biol. Chem. 279*, 45618−45625.
11. Birck, M. R., and Woodard, R. W. (2001) *Aquifex aeolicus* 3-deoxy-D-*manno*-2-octulosonic acid 8-phosphate synthase: a new class of KDO 8-P synthase?, *J. Mol. Evol. 52*, 205−214.
12. Duewel, H. S., and Woodard, R. W. (2000) A metal bridge between two enzyme families. 3-deoxy-D-*manno*-octulosonate 8-phosphate synthase from *Aquifex aeolicus* requires a divalent metal for activity, *J. Biol. Chem. 275*, 22824−22831.
13. Radaev, S., Dastidar, P., Patel, M., Woodard, R. W., and Gatti, D. L. (2000) Structure and mechanism of 3-deoxy-D-*manno*-octulosonate 8-phosphate synthase, *J. Biol. Chem. 275*, 9476−9484.
14. Wagner, T., Kretsinger, R. H., Bauerle, R., and Tolbert, W. D. (2000) 3-Deoxy-D-*manno*-octulosonate-8-phosphate synthase from *Escherichia coli*. model of binding of phosphoenolpyruvate and D-arabinose-5- phosphate, *J. Mol. Biol. 301*, 233−238.
15. Vainer, R., Belakhov, V., Rabkin, E., Baasov, T., and Adir, N. (2005) Crystal structures of *Escherichia coli* KDO8P synthase complexes reveal the source of catalytic irreversibility, *J. Mol. Biol. 351*, 641−652.
16. Wang, J., Duewel, H. S., Stuckey, J. A., Woodard, R. W., and Gatti, D. L. (2002) Function of His185 in *Aquifex aeolicus* 3-deoxy-D-*manno*-octulosonate 8-phosphate synthase, *J. Mol. Biol. 324*, 205−214.
17. Xu, X., Kona, F., Wang, J., Lu, J., Stemmler, T., and Gatti, D. L. (2005) The catalytic and conformational cycle of *Aquifex aeolicus* KDO8P synthase: role of the L7 loop, *Biochemistry 44*, 12434−12444.
18. Asojo, O., Friedman, J., Adir, N., Belakhov, V., Shoham, Y., and Baasov, T. (2001) Crystal structures of KDOP synthase in its binary complexes with the substrate phosphoenolpyruvate and with a mechanism-based inhibitor, *Biochemistry 40*, 6326−6334.
19. Kaustov, L., Kababya, S., Du, S., Baasov, T., Gropper, S., Shoham, Y., and Schmidt, A. (2000) Structural and mechanistic investigation of 3-deoxy-D-*manno*-octulosonate-8-phosphate synthase by solid-state REDOR NMR, *Biochemistry 39*, 14865−14876.
20. Li, J., Wu, J., Fleischhacker, A. S., and Woodard, R. W. (2004) Conversion of *Aquifex aeolicus* 3-deoxy-D-*manno*-octulosonate 8-phosphate synthase, a metalloenzyme, into a nonmetalloenzyme, *J. Am. Chem. Soc. 126*, 7448−7449.
21. Oliynyk, Z., Briseno-Roa, L., Janowitz, T., Sondergeld, P., and Fersht, A. R. (2004) Designing a metal-binding site in the scaffold of *Escherichia coli* KDO8PS, *Protein Eng., Des. Sel. 17*, 383−390.
22. Shulami, S., Furdui, C., Adir, N., Shoham, Y., Anderson, K. S., and Baasov, T. (2004) A reciprocal single mutation affects the metal requirement of 3-deoxy-D-*manno*-2-octulosonate-8-phosphate (KDO8P) synthases from *Aquifex pyrophilus* and *Escherichia coli*, *J. Biol. Chem. 279*, 45110−45120.
23. Nozaki, Y. (1972) The preparation of guanidine hydrochloride, *Methods Enzymol. 26* (Part C), 43−50.
24. Royer, C. A., Mann, C. J., and Matthews, C. R. (1993) Resolution of the fluorescence equilibrium unfolding profile of trp aporepressor using single tryptophan mutants, *Protein Sci. 2*, 1844−1852.
25. Fersht, A. (1999) *Structure and Mechanism in Protein Science: A Guide to Enzyme Catalysis and Protein Folding*, W. H. Freeman, New York.
26. Duggleby, R. G. (1995) Analysis of enzyme progress curves by nonlinear regression, *Methods Enzymol. 249*, 61−90.
27. Beechem, J. M. (1992) Global analysis of biochemical and biophysical data, *Methods Enzymol. 210*, 37−54.
28. Kuzmic, P. (1996) Program DYNAFIT for the analysis of enzyme kinetic data: application to HIV proteinase, *Anal. Biochem. 237*, 260−273.
29. Bates, D. M., and Watts, D. G. (1998) *Nonlinear Regression Analysis and its Applications*, Wiley, New York.
30. Duewel, H. S., Sheflyan, G. Y., and Woodard, R. W. (1999) Functional and biochemical characterization of a recombinant 3-deoxy-D-*manno*-octulosonic acid 8-phosphate synthase from the hyperthermophilic bacterium *Aquifex aeolicus*, *Biochem. Biophys. Res. Commun. 263*, 346−351.
31. Otwinowski, Z., and Minor, W. (1997) Processing of X-ray diffraction data collected in oscillation mode, *Methods Enzymol. 276*, 307−326.
32. Adams, P. D., Pannu, N. S., Read, R. J., and Brunger, A. T. (1997) Cross-validated maximum likelihood enhances crystallographic simulated annealing refinement, *Proc. Natl. Acad. Sci. U.S.A. 94*, 5018−5023.
33. Goldenberg, D. P. (1992) Mutational analysis of protein folding and stability, in *Protein Folding* (Creighton, T. E., Ed.) pp 353−403, W. H. Freeman, New York.
34. Shortle, D., and Meeker, A. K. (1986) Mutant forms of staphylococcal nuclease with altered patterns of guanidine hydrochloride and urea denaturation, *Proteins 1*, 81−89.
35. Segel, I. (1975) *Enzyme Kinetics. Behavior and Analysis of Rapid Equilibrium and Steady-State Enzyme Systems*, John Wiley & Sons, New York.
36. King, E. L., and Altman, C. (1956) A schematic method of deriving the rate laws for enzyme-catalyzed reactions, *J. Phys. Chem. 60*, 1375−1378.
37. Cornish-Bowden, A. (1995) *Fundamentals of Enzyme Kinetics*, revised ed., Portland Press, London.
38. Cleland, W. W. (1963) The kinetics of enzyme-catalyzed reactions with two or more substrates or products. III. Prediction of initial velocity and inhibition patterns by inspection, *Biochim. Biophys. Acta 67*, 188−196.
39. Bevington, P. R. (1969) *Data Reduction and Error Analysis for the Physical Sciences*, McGraw-Hill, New York.
40. Ray, P. H. (1980) Purification and characterization of 3-deoxy-D-*manno*-octulosonate 8-phosphate synthetase from *Escherichia coli*, *J. Bacteriol. 141*, 635−644.
41. Howe, D. L., Sundaram, A. K., Wu, J., Gatti, D. L., and Woodard, R. W. (2003) Mechanistic insight into 3-deoxy-D-*manno*-octulosonate-8-phosphate synthase and 3-deoxy-D-*arabino*-heptulosonate-7-phosphate synthase utilizing phosphorylated monosaccharide analogues, *Biochemistry 42*, 4843−4854.
42. Shumilin, I. A., Bauerle, R., and Kretsinger, R. H. (2003) The high-resolution structure of 3-deoxy-D-*arabino*-heptulosonate-7-phosphate synthase reveals a twist in the plane of bound phosphoenolpyruvate, *Biochemistry 42*, 3766−3776.
43. Shumilin, I. A., Bauerle, R., Wu, J., Woodard, R. W., and Kretsinger, R. H. (2004) Crystal structure of the reaction complex of 3-deoxy-D-*arabino*-heptulosonate-7-phosphate synthase from *Thermotoga maritima* refines the catalytic mechanism and indicates a new mechanism of allosteric regulation, *J. Mol. Biol. 341*, 455−466.
44. Jensen, R. A., Xie, G., Calhoun, D. H., and Bonner, C. A. (2002) The correct phylogenetic relationship of KdsA (3-deoxy-D-*manno*-octulosonate 8-phosphate synthase) with one of two independently evolved classes of AroA (3-deoxy-D-*arabino*-heptulosonate 7-phosphate synthase), *J. Mol. Evol. 54*, 416−423.

BI6024879

Supporting Information

A. Thermal denaturation of the enzymes of the C11N series.

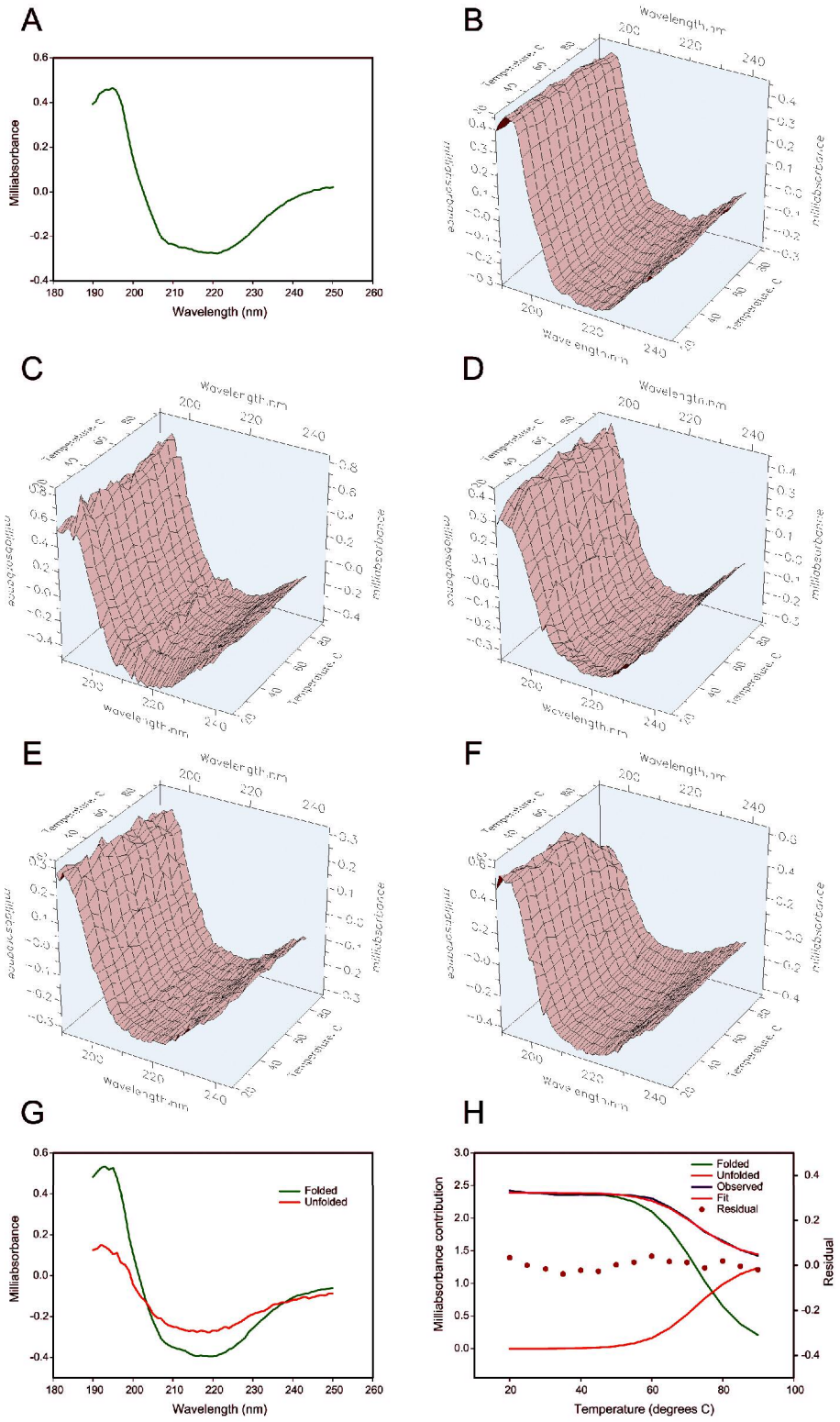

Fig. 1. Thermal denaturation of wild-type and mutant KDO8PS. A. CD spectrum of wild-type KDO8PS in the 190-250 nm region. Panels B through F show the spectral changes in the CD spectrum of wild-type KDO8PS (B), C11N (C), P10/C11N (D), C11N/S235P/Q237A (E), and P10M/C11N/S235P/Q237A during a temperature ramp from 20 to 90°C. G. SVD deconvolution of the thermal denaturation of P10M/C11N/S235P/Q237A, showing the two primary components (folded and unfolded protein) of all the spectra. Panel H shows that essentially all the spectral changes occurring during the thermal denaturation are accounted for by a linear combination of the two primary spectral components with minimal residual (see the almost perfect correspondence between the calculated and the observed cumulative spectral amplitude).

B. Chemical denaturation of the enzymes of the C11N series.

GdnHCl denaturation curves were obtained for the wild type and mutant KDO8PS's. Purified recombinant protein was incubated overnight with increasing GdnHCl concentrations at 23°C. The red shifts in intrinsic fluorescence emission spectra at increasing GdnHCl concentrations were quantified as the intensity-averaged emission wavelength, λ_{avg} (*1*), calculated according to Equation (1), where λ_i and I_i are the emission wavelength and its corresponding fluorescence intensity at that wavelength.

$$\lambda_{avg} = \sum I_i \lambda_i \Big/ \sum I_i \qquad (1)$$

Baseline and transition-region data for the GdnHCl equilibrium denaturation curve were fitted to a two-state linear-extrapolation model (*2*) according to Equation (2),where ΔG_u is the free energy change for unfolding at a given denaturant (GdnHCl) concentration, ΔG^{H_2O} is the free energy change for unfolding in the absence of denaturant, m is a slope term that equates the change in ΔG_u per unit concentration of GdnHCl, R is the gas constant (1.987 cal mol^{-1} K^{-1}), T is the temperature (296.15 K), and K_u is the equilibrium constant for unfolding.

$$\Delta G_u = \Delta G^{H_2O} - m[D] = -RT \ln K_u \qquad (2)$$

From Equation (2) it follows that $\Delta G^{H_2O} = m[D]_{50\%}$. The linear-extrapolation model expresses the signal (λ_{avg}) as a function of GdnHCl concentration according to Equation (3) (*3*), where y_i is the observed signal, y_N and y_D are the baseline intercepts corresponding to, respectively, native and denatured proteins, m_N and m_D are the corresponding baseline slopes, $[X]_i$ is the denaturant

concentration corresponding to the *i*th addition, *m* is the slope of a ΔG unfolding *versus* [X] plot, R and *T* are the gas constant and temperature as defined above. $[D]_{50\%}$ is the denaturant (GdnHCl) concentration at the midpoint of the transition, in which there is an equal amount of the folded and unfolded protein ($K_u = 1$).

$$y_i = \frac{y_N + m_N[X]_i + (y_D + m_D[X]_i)\exp\left[m([X]_i - [D]_{50})/RT\right]}{1 + \exp\left[m([X]_i - [D]_{50\%})/RT\right]} \quad (3)$$

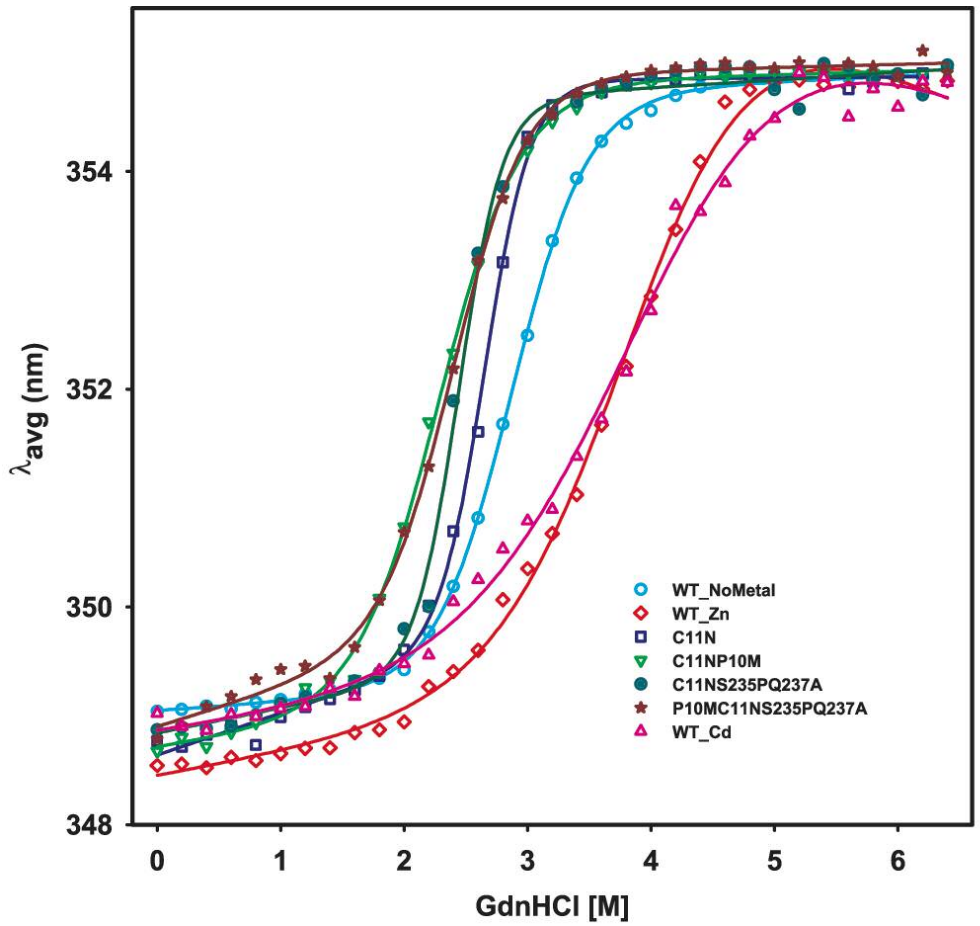

Fig. 2. Chemical denaturation of wild-type and mutant KDO8PS. The position of each point on the ordinate axis represents the value of the intensity-averaged emission wavelength (λ_{avg})

of the protein at a certain GdnHCl concentration. Fits to the experimental points are shown as continuous lines.

C. Kinetic analysis of the enzymes of the C11N series.

The enzyme reactions catalyzed by KDO8PS (Fig. 3, see below) can be written as a set of biochemical equations in which the first rate constant listed after a given step corresponds to the left-to-right (forward) step and the second rate constant corresponds to the right-to-left (reverse) step.

$E + PEP \rightarrow E\bullet PEP$	k_1	
$E\bullet PEP \leftrightarrow E\bullet PEP\bullet A5P$	k_2	k_{-2}
$E\bullet PEP + R5P \leftrightarrow E\bullet PEP\bullet R5P$	k_2^{R5P}	k_{-2}^{R5P}
$E\bullet PEP\bullet R5P \rightarrow E\bullet R5P + 2PGA$	k_3^{R5P}	
$E\bullet PEP\bullet A5P \rightarrow E\bullet KDO8P + P_i$	k_3	
$E\bullet KDO8P \leftrightarrow E + KDO8P$	k_4	k_{-4}
$E + A5P \leftrightarrow E\bullet A5P$	k_5	k_{-5}
$E + R5P \leftrightarrow E\bullet R5P$	k_5^{R5P}	k_{-5}^{R5P}
$E + P_i \leftrightarrow E\bullet P_i$	k_6	k_{-6}
$E\bullet PEP + P_i \leftrightarrow E\bullet PEP\bullet P_i$	k_7	k_{-7}

The system of simultaneous first-order ordinary differential equations (4a-o) that describes the time-course of these reactions was automatically derived by the DynaFit software, and used in the least-squares regression of experimental data employing Reich's modification of the Levenberg-Marquardt Algorithm (*4*).

$$d[E]/dt = -k_1[E][PEP]+k_4[E\bullet KDO8P]-k_{-4}[E][KDO8P]-k_5[E][A5P]+k_{-5}[E\bullet A5P]-k_5^{R5P}[E][R5P] + k_{-5}^{R5P}[E\bullet R5P]-k_6[E][P_i]+k_{-6}[E\bullet P_i] \quad (4a)$$

$$d[A]/dt = -k_1[E][PEP] \quad (4b)$$

$$d[E\bullet PEP]/dt = +k_1[E][PEP]-k_2[E\bullet PEP][A5P]+k_{-2}[E\bullet PEP\bullet A5P]-k_2^{R5P}[E\bullet PEP][R5P]$$

$$+k_{-2}^{R5P}[E\bullet PEP\bullet R5P]-k_7[E\bullet PEP][P_i]+k_{-7}[E\bullet PEP\bullet P_i] \quad (4c)$$

$$d[A5P]/dt = -k_2[E\bullet PEP][A5P]+k_{-2}[E\bullet PEP\bullet A5P]-k_5[E][A5P]+k_{-5}[E\bullet A5P] \quad (4d)$$

$$d[E\bullet PEP\bullet A5P]/dt = +k_2[E\bullet PEP][A5P]-k_{-2}[E\bullet PEP\bullet A5P]-k_3[E\bullet PEP\bullet A5P] \quad (4e)$$

$$d[R5P]/dt = -k_2^{R5P}[E\bullet PEP][R5P]+k_{-2}^{R5P}[E\bullet PEP\bullet R5P]-k_5^{R5P}[E][R5P]+k_{-5}^{R5P}[E\bullet R5P] \quad (4f)$$

$$d[E\bullet PEP\bullet R5P]/dt = +k_2^{R5P}[E\bullet PEP][R5P]-k_{-2}^{R5P}[E\bullet PEP\bullet R5P]-k_3^{R5P}[E\bullet PEP\bullet R5P] \quad (4g)$$

$$d[E\bullet R5P]/dt = +k_3^{R5P}[E\bullet PEP\bullet R5P]+k_5^{R5P}[E][R5P]-k_{-5}^{R5P}[E\bullet R5P] \quad (4h)$$

$$d[2PGA]/dt = +k_3^{R5P}[E\bullet PEP\bullet R5P] \quad (4i)$$

$$d[E\bullet KDO8P]/dt = +k_3[E\bullet PEP\bullet A5P]-k_4[E\bullet KDO8P]+k_{-4}[E][KDO8P] \quad (4j)$$

$$d[P_i]/dt = +k_3[E\bullet PEP\bullet A5P]-k_6[E][P_i]+k_{-6}[E\bullet P_i]-k_7[E\bullet PEP][P_i]+k_{-7}[E\bullet PEP\bullet P_i] \quad (4k)$$

$$d[KDO8P]/dt = +k_4[E\bullet KDO8P]-k_{-4}[E][KDO8P] \quad (4l)$$

$$d[E\bullet A5P]/dt = +k_5[E][B]-k_{-5}[E\bullet A5P] \quad (4m)$$

$$d[E\bullet P_i]/dt = +k_6[E][P_i]-k_{-6}[E\bullet P_i] \quad (4n)$$

$$d[E\bullet PEP\bullet P_i]/dt = +k_7[E\bullet PEP][P_i]-k_{-7}[E\bullet PEP\bullet P_i] \quad (4o)$$

The corresponding system of equations that describes the reaction with only PEP and A5P is easily obtained by removing all the terms that contain R5P. In this particular case, global least-squares fit was based on the stepwise refinement of all adjustable model parameters. In the first stage of the analysis, rate constants and protein concentrations were refined. In the second stage, protein concentrations were fixed at the refined values, and PEP concentrations were refined. In the third stage, protein and PEP concentrations were fixed at the refined values and A5P concentrations were refined. In the fourth stage protein, PEP and A5P concentrations were fixed at the refined values and P_i concentrations were refined. In the fifth and final stage, all concentrations were fixed at the refined values and only the rate constants were refined. Each progress curve consisted of 100 points, for a total of 1900 points. In the case of reactions occurring in the presence of both A5P and R5P the rate constants for the steps involving A5P were fixed at the values identified in the above experiments and only the rate constants related to steps involving R5P were refined.

As an example, the concentrations of substrates used, and the experimental and least-squares fit progress curves for both the wild type and the C11N mutant are shown respectively in Table 1 and Fig. 3.

Table 1. Initial concentrations (μM) of substrates and products in the reaction progress curves shown in Figure 3, catalyzed by the wild-type and C11N enzymes.

		Wild Type				C11N			
Figure 3 panels	Progress Curve	PEP	A5P	R5P	P_i	PEP	A5P	R5P	P_i
A, B	1	93	193	0	0	100	192	0	0
	2	96	293	0	0	95	287	0	0
	3	185	290	0	0	187	262	0	0
	4	123	575	0	0	141	384	0	0
	5	278	578	0	0	266	472	0	0
	6	409	571	0	0	377	566	0	0
	7	243	94	0	0	174	114	0	0
	8	293	141	0	0	275	223	0	0
	9	377	194	0	0	326	203	0	0
	10	480	89	0	0	434	111	0	0
	11	376	228	0	0	333	251	0	0
	12	475	277	0	0	341	288	0	0
	13	572	419	0	0	508	406	0	0
	14	440	97	0	600	519	106	0	600
	15	488	98	0	900	429	110	0	900
	16	98	195	0	300	102	195	0	300
	17	97	196	0	600	100	195	0	600
	18	480	97	0	2000	450	109	0	2000
	19	244	348	0	4000	100	195	0	4000

Table 1. cont.

		Wild Type				C11N			
Figure 3 panels	Progress Curve	PEP	A5P	R5P	P_i	PEP	A5P	R5P	P_i
C, D	1	286	100	50	0	283	100	50	0
	2	289	100	100	0	284	100	100	0
	3	285	100	150	0	287	100	150	0
	4	299	100	200	0	285	100	200	0
	5	284	100	250	0	286	100	250	0
	6	283	100	300	0	295	100	300	0
	7	299	200	50	0	-	-	-	-
	8	313	200	100	0	295	200	100	0
	9	291	200	150	0	286	200	150	0
	10	290	200	200	0	290	200	200	0
	11	287	200	250	0	294	200	250	0
	12	-	-	-	-	294	200	300	0
	13	51	0	27	0	-	-	-	-
	14	53	0	66	0	-	-	-	-
	15	111	0	100	0	-	-	-	-
	16	46	0	262	0	-	-	-	-
	17	31	0	132	0	-	-	-	-

The enzyme concentration was 2 μM with the exception of the last 5 experiments, in which it was 5 μM. All substrates and products concentrations are in units of μM.

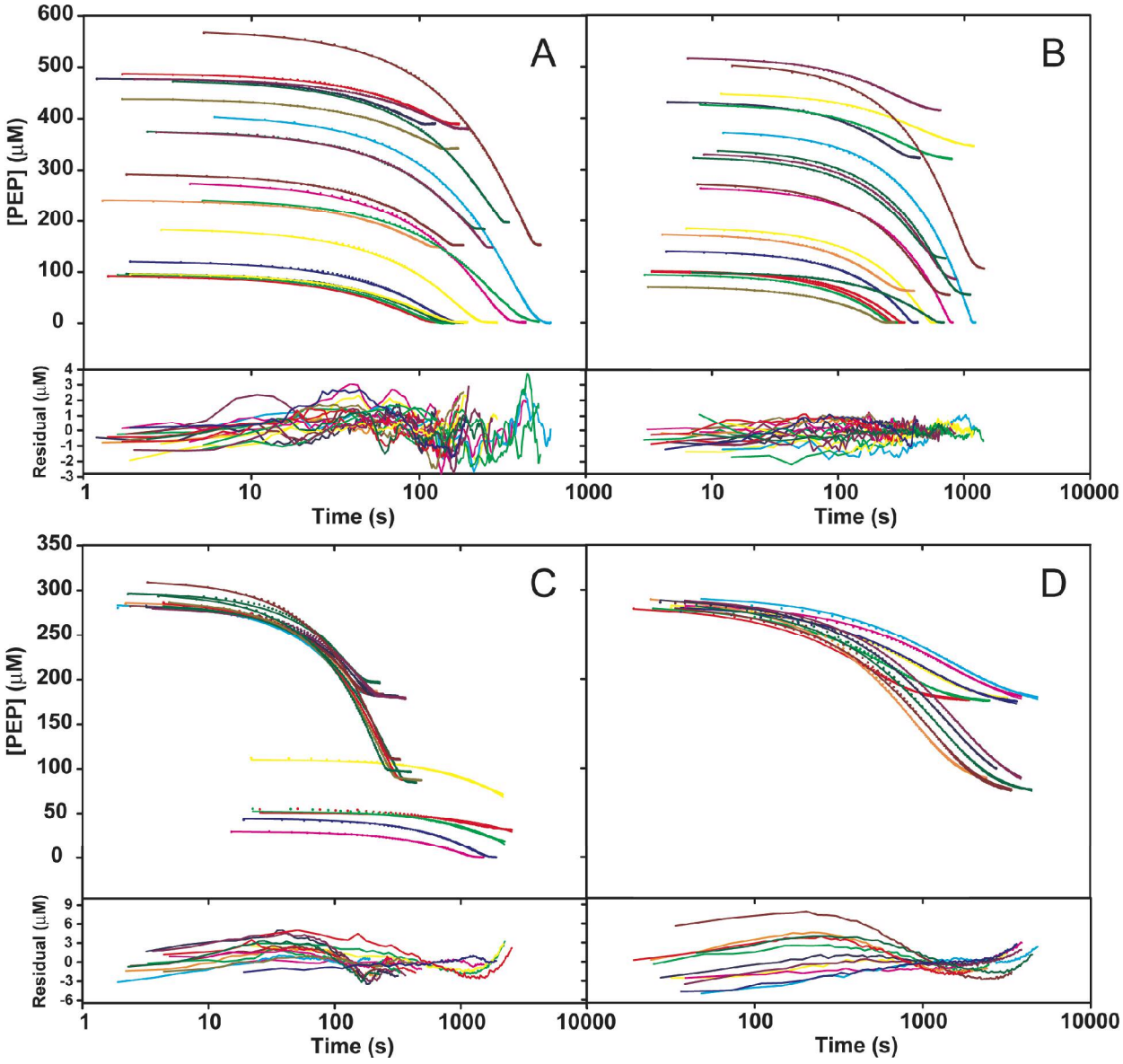

Fig. 3. Progress curves of PEP consumption by the wild-type and C11N enzyme in the presence of A5P (A, B panels) or A5P and R5P (C, D panels). The spectrophotometric signal collected at 232 nm is already converted into PEP concentrations (ε^{PEP} = 2840 M^{-1} cm^{-1}). Experimental points and least-squares fit curves are shown as filled circles and solid lines, respectively. The best-fit model progress curves obtained in the presence of both A5P and R5P were generated assuming production of both KDO8P and 2-PGA. Notice the slow futile cycle of PEP

consumption when only R5P is present (bottom traces in panel C). In order to display the quality of the fit in both short and long traces, a log scale is used for the time axis. The residual plots, representing the differences between the least-squares model curves and the experimental data, are shown in the smaller panels under each plot.

D. Structure of P10M/C11N in complex with PEP

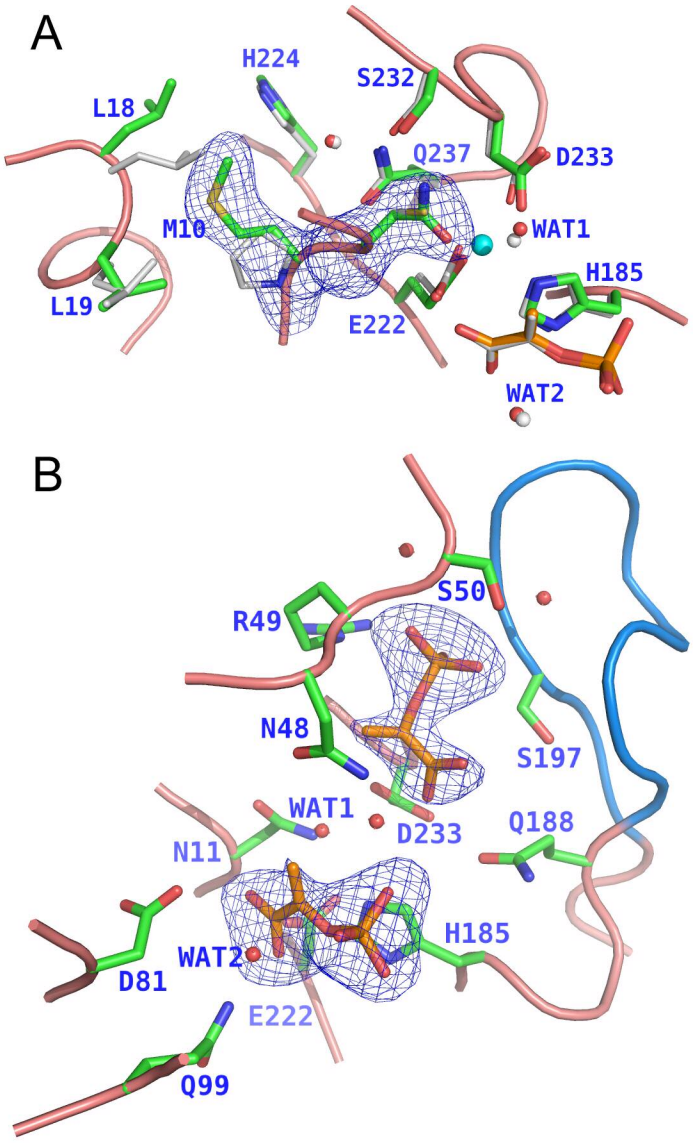

Fig. 4. A. P10M/C11N mutant in complex with PEP. The structure of the double mutant (green bonds) is shown superimposed to the structure of the wild type (white bonds/spheres). The largest differences occur at Leu-18 and Leu-19. The active site metal in the wild-type enzyme is shown as a cyan sphere. PEP is shown with orange bonds. B. One of the subunits in which PEP (orange bonds) binds also at the A5P site. This second molecule of PEP displays a different geometry with the enol plane almost perpendicular to the carboxylate plane. In this active site the

L7 loop (colored in light blue) is closed. All electron density maps are $|F_o-F_c|$ σA omit maps contoured at 3σ.

E. Structure of C11N/S235P/Q237A in complex with PEP.

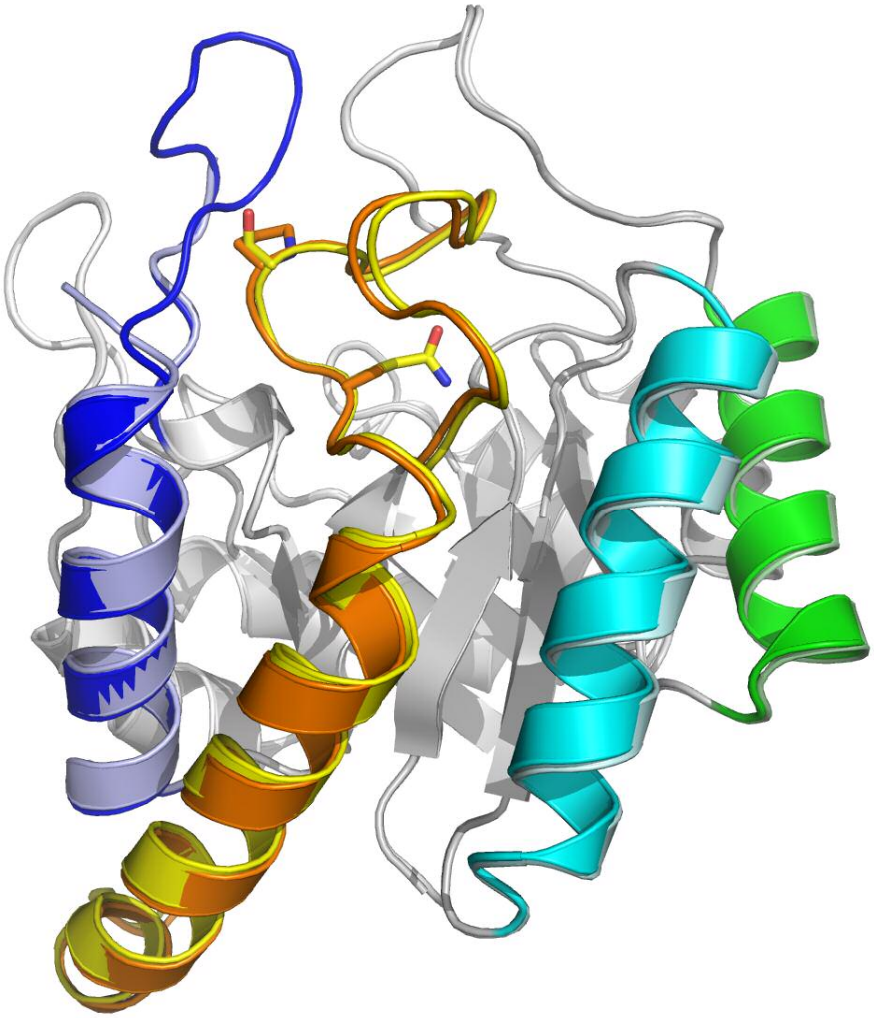

Fig. 5. Crystal form B of the C11N/S235P/Q237A mutant enzyme. A. A ribbon drawing of one of the 12 monomers contained in the asymmetric unit is shown superimposed to the structure of the wild-type enzyme. The L8 loop (residues 225-240) and the H8 helix are shown in orange (mutant) and yellow (wild type). Structural perturbations extend from the mutation site (L8) also to the nearby H7 (dark blue [mutant] and light blue [wild type]), H1 (dark cyan [mutant] and light cyan [wild type]), and H2 (dark green [mutant] and light green [wild type]).

F. Structural variation between subunits in the enzymes of the C11N series.

Table 2. RMS deviations (Å) between the subunits of the C11N series mutants and the wild type enzyme. The reference structures for wild-type *A. aeolicus* KDO8PS in complex with PEP and PEP + A5P are 1FWS and 1FWW, respectively.

	C11N + PEP		C11N + PEP + A5P		P10M/C11M + PEP		C11M/S235P/Q237A + PEP		C11M/S235P/Q237A + PEP + A5P (C form)		C11M/S235P/Q237A + PEP + A5P (D form)		P10M/C11M/S235P/Q237A + PEP + A5P	
	WT A	WT B	WT A	WT B	WT A	WT B	WT A	WT B	WT A	WT B	WT A	WT B	WT A	WT B
A	0.107	0.278	0.124	0.198	0.261	0.256	0.239	0.239	0.257	0.249	0.137	0.197	0.167	0.228
B	0.194	0.126	0.198	0.129	0.316	0.312	0.268	0.265	0.265	0.270	0.217	0.168	0.227	0.208
C					0.315	0.323	0.251	0.253	0.249	0.269				
D					0.305	0.290	0.259	0.199	0.271	0.244				
E					0.343	0.352	0.252	0.244	0.287	0.282				
F					0.331	0.347	0.288	0.268	0.289	0.281				
G					0.321	0.337	0.235	0.237	0.264	0.263				
H					0.329	0.339	0.276	0.271	0.263	0.270				
I					0.291	0.295	0.229	0.237	0.241	0.245				
J					0.274	0.270	0.272	0.231	0.265	0.257				
K					0.363	0.368	0.240	0.229	0.291	0.286				
L					0.356	0.344	0.290	0.255	0.285	0.262				

References:

(1) Royer, C. A., Mann, C. J., and Matthews, C. R. (1993) Resolution of the fluorescence equilibrium unfolding profile of trp aporepressor using single tryptophan mutants. *Protein Sci 2*, 1844-52.

(2) Fersht, A. (1999) *Structure and Mechanism in Protein Science: A Guide to Enzyme Catalysis and Protein Folding*, W H Freeman & Co.

(3) Clarke, J., and Fersht, A. R. (1993) Engineered disulfide bonds as probes of the folding pathway of barnase: increasing the stability of proteins against the rate of denaturation. *Biochemistry 32*, 4322-9.

(4) Reich, J. G. (1992) *Curve fitting and modelling for scientists and engineers.*, McGraw-Hill, New York.